Research Paper

pn Heterojunctions in NiO:TiO₂ composites with type-II band alignment assisting sunlight driven photocatalytic H₂ generation

Sushma A. Rawool[a,1], Mrinal R. Pai[a,1,*], Atindra M. Banerjee[a], Ashok Arya[b,1], R.S. Ningthoujam[a,1], R. Tewari[b,1], Rekha Rao[c,1], Bhagyashree Chalke[d], Pushan Ayyub[d], A.K. Tripathi[a,1], Shyamala R. Bharadwaj[a]

[a] Chemistry Division, Bhabha Atomic Research Centre, Mumbai 400085, India
[b] Materials Science Division, Bhabha Atomic Research Centre, Mumbai 400085, India
[c] Solid State Physics Division, Bhabha Atomic Research Centre, Mumbai 400085, India
[d] Department of Condensed Matter Physics and Materials Science, Tata Institute of Fundamental Research, Homi Bhabha Road, Mumbai 400005, India

ARTICLE INFO

ABSTRACT

To accentuate the role of *pn* heterojunctions in composites, the photocatalytic properties of two composites NTC11 (NiO and TiO₂ in 1:1 molar ratio) and NTC36 (0.35:0.65) were investigated in detail for H₂ evolution reaction and compared with the component pure oxides, NiO, TiO₂ and NiTiO₃ prepared by sol-gel route. Among all samples, NTC11 was distinctly most active (greater than pure TiO₂ by ∼ 22 times, NiO has negligible activity) and yielded reproducible H₂ yields for 60 h under repetitive cycles in sunlight confirming its photostability. Maximum photocatalytic Hydrogen yield @ 0.6 l/h/m² with apparent quantum efficiency (AQE) of 5.4% and solar fuel efficiency (SFE) of 0.8% under sunlight and 1.4 l/h/m² with AQE of 7.8% under UV–vis irradiation along with evolution of bubbles was observed over Pt(1 wt%)/NTC11. Synthesis conditions, calcination temperature and phase compositions were very critical and played an essential role in determining the overall hydrogen yield. Presence of NiTiO₃ was found to be derogatory for the photocatalytic activity of NTC36.

The key factors responsible for enhanced rate of sunlight assisted hydrogen generation over NTC11 were 1. Formation of *pn* nanojunctions in NTC11 evident by enhanced life times of charge carriers monitored by time resolved photoluminescence, uniform distribution of NiO and TiO₂ nanoparticles with Ni/Ti in ratio of 0.99 and 0.95 at bulk and surface, respectively. 2. Favourable morphological characteristics: monodisperse, nanosized faceted particles, higher surface area, better porosity and pore volume. 3. Coformation of minimal NiTiO₃ phase. 4. First principles calculations by density functional theory (DFT) over pure NiO revealed it's electronic and band structure that helped in understanding its behavior as PL quencher and its contribution in visible light absorption of composites, 5. Valence band offset (ΔE_v) and conduction band offset (ΔE_c) at NiO and TiO₂ heterojunction was calculated to be 0.53 eV and 0.93 eV, respectively. 6. Type-II band alignment was derived at the interface and mechanism was proposed, 7. The effective forbidden gap was deduced to be $3.2(E_{g,TiO2}) - \Delta E_v = 3.6(E_{g\,NiO}) - \Delta E_c = 2.67$ eV. Thus, a composite of *pn* oxides offers lower band gap energy of 2.67 eV as compared to both pure oxides TiO₂ and NiO with effectiveness in charge separation across the *pn* junction leading to efficient improved photocatalyst.

1. Introduction

Till date there are innumerable reports on generation of H₂ using titanium dioxide, TiO₂/modified TiO₂ photocatalysts. Evidently, post Honda-Fujishima [1] classical experiment, vigorous research on TiO₂ suggests that it is a potential photocatalyst for designing futuristic commercial solar photocatalytic systems. Several prototypes have been developed in which TiO₂ based photocatalysts were deployed for demonstrating large scale H₂ production in photoreactors coupled with compound parabolic concentrators (CPC) for efficient utilization of solar energy [2,3]. We also endeared to demonstrate enhanced hydrogen generation in upscaled photoreactors over Cu/TiO₂ photocatalysts under sunlight after optimizing several parameters such as amount of photocatalyst, illumination area and form of the

photocatalyst [4]. It is noteworthy that research on titanium oxide based photocatalysts is swiftly progressing from laboratory to land due to its favourable properties. Yet, the goals of harnessing sunlight with required solar fuel efficiencies are not achieved and design of cheap stable and sufficiently active photocatalyst is still awaited.
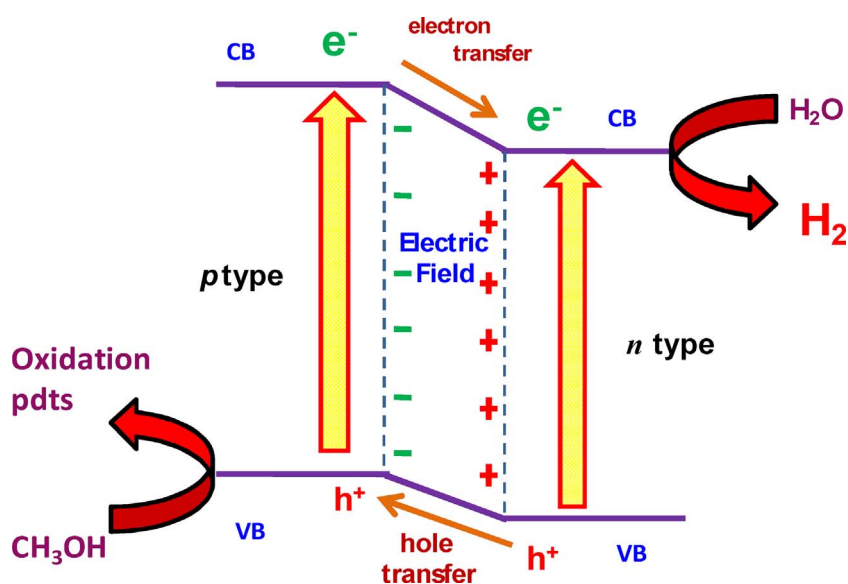
TiO$_2$ is an attractive material for harvesting solar energy owing to its optical and electronic properties, high resistance to photocorrosion, stable to wide range of pH, non-toxic and low cost. Nevertheless, the photocatalytic activity is constrained by two main factors: the inability to absorb visible light and the fast recombination of photogenerated electron and hole [5]. Extensive literature is available on extending the photoresponse of TiO$_2$ in visible region by various methods such as incorporation of anionic dopants viz; N [6], C [7], and S [8], cationic dopants which are generally transition metal or rare earth ions, structural defects such as Ti^{3+} and oxygen vacancies, co-doping or forming composite with low band gap material, noble metal loading, dye sensitization, surface modification [5–9].

To impede the e$^-$/h$^+$ recombination, commonly used strategies were forming metal-semiconductor interface where metal acts as electron trap centre, improving crystallinity to reduce defects which otherwise acts as recombination centers and generation of internal electric field through *pn* or polymorph junctions [10]. Studies have revealed that synergestic effects prevail between *p* and *n* type semiconductors in composites leading to important electrical, optical properties and improved separation of photogenerated holes and electrons [11–14]. TiO$_2$ is well known for its photocatalytic activity and it behaves as *n*-type semiconductor due to loss of lattice oxygen. Nickel oxide (NiO) is a *p*-type semiconductor and it is widely used as hydrogenation catalyst [15], gas sensor [16], its indirect band gap is 3.6 eV [17] still it shows absorbance in visible light due to *d-d* transition. A combination of *p* and *n*-type oxides in a composite sample induces *pn* junctions and a generalized proposed mechanism of charge separation over these two oxides is shown in Scheme 1.

The effect of *pn* junction can be verified using electric voltammetry where the photocurrent would be enhanced under forward bias in the presence of *pn* film [18,19]. Another novel *pn* junction, Ag$_3$PO$_4$/BiPO$_4$ photocatalyst was found to enhance photodegradation of methyl orange as compared to individual oxides, ascribed to highly efficient charge separation of photogenerated electron–hole pairs through *pn* heterojunction [20]. NiO based photocatalysts have applications in photodegradation of dyes and pigments [18,21], photocatalytic reduction of hexavalent chromium, Cr$_2$O$_7$$^{2-}$ in aqueous solution [22,23], photodegradation of harmful chemicals such as *p*-chlorophenol or gaseous

acetaldehyde under UV light irradiation [24,25]. In spite of extensive investigations on photodegradation and photoreduction reactions, scanty literature on evaluating the potential of NiO and TiO$_2$ system as a photocatalyst for H$_2$ generation is available [26–29]. Very recently, we have reported [4] the role of Cu ions in enhancement of photocatalytic evolution of H$_2$ from H$_2$O-methanol/glycerol mixtures over Cu/Ti oxides and in upscaled photo-reactors under sunlight. Similarly, effect of different transition metal ions (Fe^{3+}, Cr^{3+}, Ni^{2+}) and rare earth ion (Nd^{3+}) substitution were compared in enhancing the apparent quantum efficiency of novel indium titanate oxide photocatalyst was reported by us [30–34].

In the present study, efforts were undertaken to prepare almost NiTiO$_3$ free NiO-TiO$_2$ composites and after thorough characterization their photocatalytic properties were evaluated in sunlight, visible and UV–vis irradiation for decomposition of water. Nano-composites of NiO-TiO$_2$ in (1:1) and (0.35:0.65) ratios, NiTiO$_3$, TiO$_2$ and NiO samples were synthesized through sol-gel method at different calcination temperatures. Co-formation of a secondary phase NiTiO$_3$ and its contribution in photocatalytic activity of NiO-TiO$_2$ composite is emphasized and supported by DFT calculations. Preparation of NiTiO$_3$ was also attempted by solid state route by using respective oxides in appropriate quantity. To establish the phase purity/composition, surface morphology, oxidation states, elemental quantification on surface and bulk, optical features, electronic properties, e$^-$h$^+$ recombination profiles, samples were characterized by X-ray diffraction (XRD), X-ray photoelectron spectroscopy (XPS), N$_2$-Brunauer, Emmett and Teller (N$_2$-BET) surface area, Raman spectroscopy, inductively coupled plasma-optical emission spectroscopy (ICP-OES), field emission-scanning electron microscopy/energy dispersive X-ray spectroscopy (FESEM/EDX), high resolution transmission electron microscopy/selected area electron diffraction spectroscopy (HR-TEM/SAED), diffuse reflectance UV–vis spectroscopy (DRS) and photoluminescence studies (PL). Band alignment at heterojunctions of NiO-TiO$_2$ oxides in composites was proposed here after calculating the valence band offset (ΔE_v) and conduction band offset (ΔE_c). Lifetimes of photoexcited electrons and holes was measured by time-resolved photoluminescence in composites and compared with single phased oxides, to emphasize the role of *pn* nanojunctions in charge carrier separation. Also, photocatalytic activity was evaluated by monitoring generation of hydrogen from water and methanol mixture in evacuated atmosphere under visible, UV–vis and natural sunlight. Effect of calcination temperature and subsequent formation of NiTiO$_3$ phase on photocatalytic activity of NiO-TiO$_2$ nanocomposites was investigated. Sustained H$_2$ evolution for 60 h under
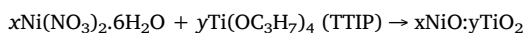

Scheme 1. A representation of pn junction model facilitating the electron–hole separation process.

sunlight and 35 h under visible light illumination was observed over most active sample. Apparent quantum efficiency (AQE) and solar fuel efficiencies (SFE) achieved are reported here.

2. Experimental

Nanoparticles of oxides TiO_2, NiO, $NiTiO_3$ and composites, $xNiO$:$yTiO_2$ ($x$moles: $y$moles = 1:1 and 0.35:0.65, abbreviated as NTC11 and NTC36 respectively) were synthesized through sol-gel method by mixing reactants in appropriate stoichiometry as depicted by following equation:

$$xNi(NO_3)_2.6H_2O + yTi(OC_3H_7)_4 \text{ (TTIP)} \rightarrow xNiO:yTiO_2$$

Nickel nitrate hexahydrate, $Ni(NO_3)_2 \cdot 6H_2O$ (> 99% Loba Chemie Pvt. Ltd.), titanium tetraisopropoxide (TTIP, 97%, Aldrich) and propan-2-ol (AR > 99.5%, SDFCL, s d fine-chem Ltd) were used as received. An appropriate amount of $Ni(NO_3)_2 \cdot 6H_2O$ was dissolved in 50 ml ethanol and 50 ml HNO_3 (5 M) to prepare solution A. Another solution referred as B containing appropriate amounts of TTIP and 30 ml of propan-2-ol was also prepared. Solution A was added drop wise to the solution B under constant stirring till a gel was formed. The gel was left overnight undisturbed for nucleation to take place. After nucleation, the gel was heated at two different temperatures viz; 90 °C (LT) and 150 °C (HT) to obtain powder. The as-synthesized powders of composite samples and TiO_2 were further calcined at 500 °C and 600 °C at a heating rate of 5 °C min⁻¹ in air to ensure the uniformity and completion of the reaction. Schematic of synthesis route is shown in Fig. S1 of Supplementary information.

Synthesis of $NiTiO_3$ was attempted by sol-gel and solid state method. The dry powder obtained after sol-gel method in the manner mentioned above was calcined at 600 °C for 10 h and at 850 °C for 5 h to obtain pure $NiTiO_3$ phase. Equimolar mixtures of NiO and TiO_2 was subjected to grinding of 40 min followed by heat treatment of 700 °C for 83 h and further heated to 1000 °C for 78 h for solid state synthesis of $NiTiO_3$. Sample was grinded at intermediate levels and reaction pathway was monitored by recording powder XRD. $NiTiO_3$ oxide was prepared by sol-gel and solid state route and abbreviated as NTOsg and NTOss respectively, in the present manuscript. $NiTiO_3$ was yellow in colour, whereas composite oxides were found to be green in colour. NTC36 is rich in $NiTiO_3$ phase and therefore has yellow colour unlike green coloured NTC11. A photograph of samples is shown in Fig. S1 of Supplementary information and Fig. 2.

1% (w/w) Pt was loaded as co-catalyst on NTC11 by photo deposition method [4].

Powder X- ray diffraction (XRD) patterns were recorded on a Philips diffractometer (model PW 1710), equipped with a graphite monochromator and Ni-filtered Cu-Kα radiation using accelerating voltage and current was 35 kV and 20 mA respectively. The crystallite size of different phases was estimated from peak broadening of the diffraction peak of corresponding phase by using Scherrer equation [4,32].

Also the weight fraction of anatase is estimated by following formula:

$$f = \frac{100}{(1 + 1.256 Ir/Ia)} \tag{1}$$

Where f is weight fraction of anatase in sample containing mixture of anatase and rutile phase, Ia & Ir is the intensity of diff raction peak of (*101*) plane of anatase phase and (*110*) plane of rutile phase [35] respectively.

XPS experiments were recorded on an electron spectrometer (SPECS, Surface Nano Analysis GmbH, Germany) using Mg-$K\alpha$ X-rays (hν = 1253.6 eV) as the primary source of radiation with an overall energy resolution of ∼0.7 eV. The appropriate corrections for charging effects were made with the help of a C 1s signal at 284.5 eV. The microstructure was studied using a Zeiss Gemini Plus field emission

scanning electron microscope (FESEM) operated at 5 kV. TEM-SAED was recorded on FEI-Tecnai G-20 microscope operating at 200 kV. The source is LaB₆ filament, the HV was at 200 kV. Sample was dispersed in methanol and a drop of it was placed on carbon coated Cu grid and solvent was evaporated at room temperature by keeping it overnight. HAADF-STEM (High Angle Annular Dark Field-Scanning Transmission Electron Microscopy) images of NTC11 were recorded using Carl zeiss Libra 200FE TEM microscope. Electron energy loss profile were recorded using incolumn EELS in TEM.

N_2- BET surface area was measured with Micromeritics ASAP 2020 V3.01 H analyzer using N_2 as the adsorbing gas. The pore size distribution based on desorption isotherm estimated by using method developed by Barret, Joyner and Halender (BJH) assuming a cylindrical pore model. The elemental analysis of Ni, Ti and Pt present in the oxide samples was evaluated using ICP-OES (*JobinVyon* JY 2000, France) after microwave digestion of ∼20 mg of the powders in concentrated HNO_3-HCl (aqua regia). Raman spectra were recorded using 532 nm lines from a diode Nd:YAG laser (power 15 mW) focused to a spot size of ∼20 μm. The scattered light was analyzed using an indigenously built 0.9 m single monochromator, coupled with a super notch filter and detected by a cooled charge couple device (CCD, Andor Technology). An optical characteristic of all samples was recorded using spectrophotometer of JASCO model V-530 (Japan) with an integrating sphere attachment in scanning range of 200–800 nm at the scanning speed of 200 nm min⁻¹. $BaSO_4$ was used as standard for recording spectra in reflectance mode. Band gap was determined by plotting Kubelka Munk function against energy and intercept on X- axis gives the band gap value of the semiconductor. Edinburgh Instruments' FLSP 920 system equipped with a 450 W Xe lamp having a Peltier element cooled red sensitive Hamamatsu R955 PMT was used to record PL with a resolution of 3 nm at room temperature. All emission spectra were corrected for the detector response. Time-resolved fluorescence measurements were carried out using a time-correlated single photon counting (TCSPC) spectrometer (Horiba Jobin Yvon, U.K.). The samples were excited by light pulses from a diode laser source (λ = 267 nm, repetition rate of 1 MHz for all samples containing TiO_2 and λ = 339 nm for pure NiO with Instrumental response function (IRF) < 0.75 ns), and the fluorescence was detected using a PMT-based detection module (model TBX4).

Photocatalytic activity of all samples was evaluated under different light illuminations: sunlight, visible and UV–vis light sources as per experimental details given in Supplementary information (Figs. S2–S5) and reported in our previous publications [4,32]. For quick reference, photocatalytic activity was evaluated in a rectangular quartz reactor of dimensions (10 × 2.1 × 2.1 cm³, 81 ml, Fig. S2b of Supplementary information), equipped with a gas sampling port for analysis and an evacuation valve. In all experiments, 0.1 g of catalyst was suspended in water + methanol mixtures (33% v/v, 15 ml). Reaction mixtures were evacuated before irradiation to provide air free conditions as oxygen acts as an electron scavenger and, on photo-adsorption, blocks the active sites for the reaction [32]. Photocatalysts suspended in water-methanol mixtures were then irradiated under different light sources. In case of experiments under sunlight, samples were photoirradiated for duration of 4–6 h during the afternoon (10.00–16.00 IST). The evolved H_2 was quantified using a gas chromatograph (model Michro-1100, Netel, India) equipped with a thermal conductivity detector (TCD), a molecular sieve column with argon as the carrier gas was employed in the isothermal temperature mode at 50 °C oven temperature. H_2 bubbles were evolved during sunlight irradiation. Similarly, bubbles were also observed during studies on Cu-TiO_2 photocatalysts and captured in a video film available online [4]. The emission spectrum of sunlight and reaction assembly in sunlight is shown in Fig. S2 of Supplementary information. The emission spectrum of visible light source with wavelengths greater than 400 nm, λ_{max} = 536 nm (medium-pressure Hg lamp, SAIC, India, 400 W) and UV–vis light source (medium-pressure Hg lamp, SAIC, India, 400 W) are shown in Figs. S3 and S4 of

Supplementary information, respectively. The reaction assembly used under UV–vis irradiation is shown in Fig. S4. The flux of both sunlight and medium pressure mercury lamps was measured using a silicon photodiode based light meter LX 1108, Lutron Electronic. Typical silicon photodiode spectral response is shown in Fig. S5 of Supplementary information. Solar flux was measured daily in the peak hours and the average recorded during 11.00–16.00 IST were used for AQE and SFE measurement. Detailed calculations of AQE and SFE are given in our previous publications [4,32].

3. First-principles theoretical calculations

Plane-wave based first-principles calculations within the density functional theory (DFT) with projector augmented wave (PAW) potentials using Vienna *Ab-initio* Simulation Package (VASP) code for calculations of ground state electronic properties of NiO (cubic, Fm3m). For partial DOS and charge transfer, we have taken Wigner-Seitz radii of Ni and O as 1.32 and 0.92 Å, respectively. Details are given in Supplementary information S1.

4. Results and discussion

XRD analysis was employed to monitor the progress of synthetic reaction, to identify the crystalline phases present and to determine crystallite size in the final product. XRD powder patterns of the samples calcined at 600 °C are shown in Fig. 1. Single phased oxides TiO_2 and NiO prepared under identical conditions are also shown for comparison (Fig. 1a and b). As expected TiO_2 calcined at 600 °C consisted of both the anatase (A) and rutile (R) phases. XRD lines due to cubic NiO (JCPDS No. 47-1049), tetragonal TiO_2 anatase (JCPDS No. 21-1272) and rutile (JCPDS No. 21-1276) were indexed in the composite samples NTC11 and NTC36 calcined at 600 °C for 10 h. In addition, extra lines appearing at $2\theta = 24.1°, 33.1°, 35.6°, 40.8°, 49.4°, 54.0°, 57.4°$ and $64.1°$ were also observed in the composite samples. These lines belonged to a secondary phase of $NiTiO_3$. To evaluate the contribution of $NiTiO_3$ phase in photocatalytic activity, a pure phase of $NiTiO_3$ was attempted by synthesized by both sol–gel (sg) and solid state (ss) routes as shown in Fig. 1e–f, respectively. Nickel titanate, $NiTiO_3$ has a rhombohedral symmetry with lattice parameters a = b = 5.030, c = 13.79 Å, vol = 302.19 Å^3 (JCPDS Card No. 33-0960). However, preparation by both methods yielded major phase of $NiTiO_3$ along with NiO and rutile as impurities. There are inherent problems with $NiTiO_3$ and phase pure product normally is not achieved as reported by many
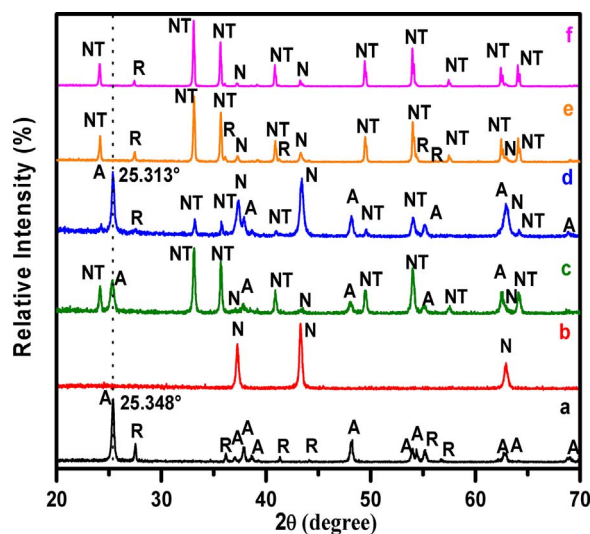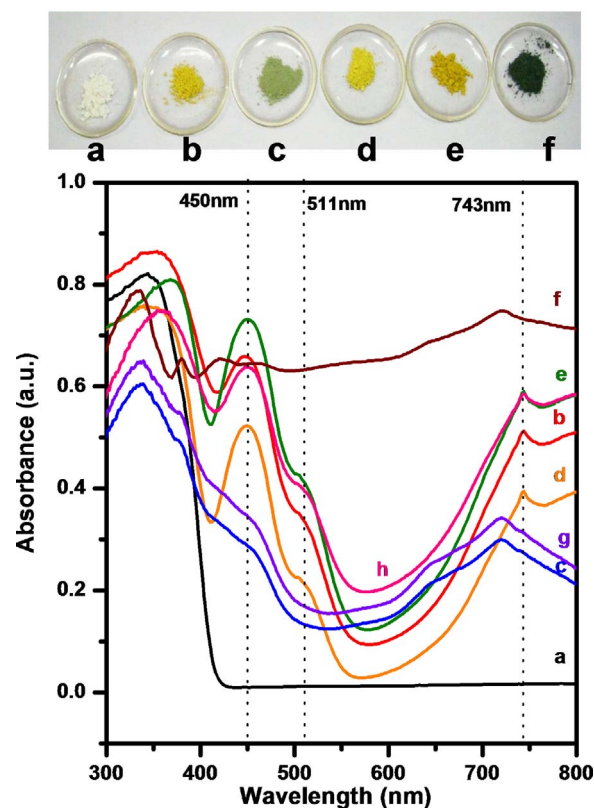

Fig. 2. Diffuse reflectance UV–vis spectra (DRS) of a. TiO_2, b. NTC36, c. NTC11, d. NTOsg, e. NTOss, f. NiO g. Used NTC11 and h. Used NTC36. Dotted lines (—) are characteristic transitions due to $NiTiO_3$ phase.

researchers [36,37]. Ruiz-Preciado et al. [37] calculated the relative content of impurities (Rutile, NiO) present in each sample prepared by sol–gel and solid state route.

Proportion of secondary phase, $NiTiO_3$ is higher in NTC36 than observed in NTC11 composite evident by comparing the intensities of XRD lines due to $NiTiO_3$ phase in curves c and d of Fig. 1. A slight peak shift of $-0.035°$ in XRD line at $2\theta = 25.348°$ due to *101* plane of anatase TiO_2 phase was observed for NTC36 oxide as compared to TiO_2 synthesized under similar conditions as shown in Fig. 1. The peak shift may be attributed to the incorporation of Ni ions at Ti site in anatase lattice.

During our investigations on Ni doped indium titanate [31] as well as by others [28] it was observed that presence of $NiTiO_3$ as impurity phase, hampers the functioning of *pn* junction of NiO-TiO_2. Co-formation of $NiTiO_3$ along with nano-junctions is undesirable. Presence of a secondary phase may act as a barrier to effective pathway of charge carriers through *pn* junction. Development of $NiTiO_3$ phase during preparation of NTC11 depends on gel drying temperature and calcinations as monitored in Fig. S6 of Supplementary information. It is reported that gel drying temperature plays an essential role in determining the phase composition [38]. Increase in gel drying temperature from 90 °C to 150 °C favours the crystallization of high temperature sintered phase, $NiTiO_3$ along with small amount of anatase TiO_2, rutile and NiO phases present in the sample, NTC11-HT 600 °C, 10 h (Fig. S6d). NTC11 samples obtained after drying the gel at lower temperature, 90 °C and calcining at 500 °C, (referred as NTC11-LT 500 °C, 5 h) yielded anatase rich composition devoid of $NiTiO_3$ phase (Fig. S6a). As calcination temperature increased to 600 °C for 3 h duration (sample referred as NTC11-LT 600 °C, 3 h), transformation of anatase to rutile was observed in addition to onset of $NiTiO_3$ phase (Fig. S6b). Further increase in duration to 10 h at 600 °C (referred as NTC11-LT 600 °C, 10 h or NTC11 throughout manuscript), resulted in well

Fig. 1. XRD patterns of a. TiO_2, b. NiO, c. NTC36, d. NTC11, e. NTOsg and f. NTOss calcined at 600 °C. ^{A} anatase, ^{R} rutile, ^{N} NiO and ^{NT} $NiTiO_3$.

crystalline powders composed of anatase TiO_2 and NiO as major phases with weak lines due to $NiTiO_3$ phase (Fig. S6c). Intensity of $NiTiO_3$ phase in curve c increased at the expense of Rutile and NiO phases (curve b) suggesting that free NiO reacted preferentially with high temperature rutile phase of TiO_2 to form nickel titanate, $NiTiO_3$. Photocatalytic activities of all these samples calcined under different conditions (Fig. S6) were evaluated and discussed later to establish structure-activity correlations. Among all samples NTC11 composite oxide (Fig. S6c) was found to be most active. Thus, gel drying temperature of 90 °C and calcination at 600 °C for 10 h are the optimized conditions that offer a well crystalline *pn* nanojunction comprised of NiO and anatase TiO_2 phases (1:1) with minimal amount of $NiTiO_3$.

The nominal compositions, identification of phases, weight fraction of anatase/rutile and crystallite size estimated from Scherrer equation for different phases present in each sample of Ni-Ti-O oxides along with their abbreviations are given in Table-S1. The average crystallite size were calculated by Scherrer equation using line width corresponding to *101* plane of anatase TiO_2, *110* plane of rutile TiO_2, *200* plane of NiO and *104* plane of $NiTiO_3$ phases present in composite and pure oxides. Anatase and NiO crystallites of 20–30 nm, whereas crystallites of 30–45 nm due to $NiTiO_3$ were present in NTC36 and NTC11 samples as listed in Table-S1. Increase in crystallite size from 17.9 nm to 43.5 nm with increase in calcination temperature from 500 °C to 600 °C respectively, was observed for pure phase of anatase TiO_2. Also, from Table-S1 it is revealed that the presence of NiO has restricted the growth of anatase crystals upto ~23 nm in NTC36 and ~31 nm in NTC11 as compared to large crystallites of ~43 nm observed for pristine TiO_2 calcined at 600 °C. Samples of $NiTiO_3$, NTOsg and NTOss consisted highly sintered crystallites with 80–81 nm and 141–143 nm size, respectively (Table-S1). It is well reported that traditional synthetic procedures yield large $NiTiO_3$ particles with low surface areas and pore volumes due to inherent problems such as high reaction temperature and heterogeneous solid phase reactions [31,39,40]. The relative ratio of anatase/rutile present in TiO_2 calcined at different temperatures and $NiTiO_3$ samples prepared by both routes (NTOss and NTOsg) and composite oxides (NTC36, NTC11), were calculated using equation mentioned in experimental section and listed in Table-S1. The TiO_2 crystallized completely in anatase phase after calcinations at 500 °C; however 25% of it got transformed into rutile after calcinations at 600 °C as listed in Table-S1. However the transition of anatase into rutile was inhibited by presence of NiO in NTC36 and NTC11 composite samples, evident by weak peak of rutile phase at $2\theta = 27.4°$, amounting to 13.9% (Table-S1). Absence of noticeable rutile peak in NTC36 cannot be explained by above reason of phase transition inhibition as very small amount of free NiO is present in NTC36. The presence of strong XRD lines due to $NiTiO_3$ phase in NTC36 sample (Fig. 1c) without any peaks due to free rutile TiO_2 and NiO phases, suggests a possibility of swiping away of whatever amount of rutile TiO_2 formed preferentially by NiO to react and produce high temperature sintered $NiTiO_3$ phase at 600 °C. As content of free NiO increases in the composite sample the transition (anatase → rutile) reaction is inhibited and crystallization of derogatory phase $NiTiO_3$ decreases. Presence of NiO in NTC11 inhibits the transformation of anatase into rutile phase and stabilizes the TiO_2 in anatase phase is in agreement with work reported by other researchers [22,41]. Possibly, slow heating of gel and availability of greater fraction of Ni ions during synthesis of NTC11, restricted the crystallization of adverse phase, $NiTiO_3$ and liberated the free NiO and TiO_2 phases, in contrast to what was observed in NTC36 where the reaction pathway leads to formation of substantial amounts of $NiTiO_3$ phase.

N_2-BET surface area, mean pore size diameter and cumulative pore volume of pristine TiO_2 is compared with composites of NiO and TiO_2 calcined at 600 °C. The comparative data is listed in Table-S2 of Supplementary information. Composite sample, NTC11 and NTC36 have shown enhanced surface area of 29.6 and 19 $m^2 g^{-1}$ respectively, and as compared to 10 $m^2 g^{-1}$ of TiO_2. The pore size distribution and cumulative pore volumes of both the samples are shown in Fig. S7 of

Supplementary information. TiO_2 is microporous with binodal distribution with maximas at 1.8 and 1.9 Å (Fig. S7a). However, these micropores coagulate to mesopores on composite formation with NiO. Mesopores in range of 11–150 Å with maxima at ~34 Å in NTC11 and still larger mesopores in range of 50–150 Å with maxima at 90 Å in NTC36 (Fig. S7b–c) were observed. A decrease in cumulative pore volume from 0.1005 $cm^3 g^{-1}$ (TiO_2) to 0.09 $cm^3 g^{-1}$ and 0.08 $cm^3 g^{-1}$ in NTC36 and NTC11, respectively was observed (Table-S2). Calcination temperature plays a very important role in deciding the resultant surface areas and porosity of oxides. Melian et al. [28] observed that surface areas of Ni/Ti oxides was between 374 and 470 $m^2 g^{-1}$ was slashed by 74% when calcined at 400 °C and by 90% at 550 °C. Similarly, pore volume of samples reduced to 0.1 $cm^3 g^{-1}$ from 0.3 $cm^3 g^{-1}$ for temperatures above 550 °C. The reduction in surface areas above 500 °C coincides with emergence of the high temperature phases such as rutile and $NiTiO_3$ at the expense of more dispersed forms such as NiO, affecting the morphological properties adversely.

Fig. S8 of Supplementary information shows Raman spectra of pure phases TiO_2, NiO, $NiTiO_3$ and compared with composite oxides, NTC11 and NTC36. According to factor group analysis, anatase TiO_2 has six Raman active modes predicted by group theory and they appear at 144 (E_g), 197 (E_g), 399 (B_{1g}), 513 (A_{1g}), 519 (B_{1g}) and 639 cm^{-1}(E_g) marked as # in Fig. S8 [42]. The two peaks of doublet (513 and 519 cm^{-1}) merges to one peak at 516 cm^{-1} at room temperature [42]. E_g, 144 cm^{-1} is the most intense and sharp vibration mode and others are weak vibrations. The rutile phase of TiO_2 has a weak band ~143 cm^{-1}. Rutile has four Raman active fundamentals, while anatase has six Raman active fundamentals [42]. Thus, the spectrum corresponds to anatase without features of rutile phase. XRD pattern of TiO_2 shows partial conversion of anatase to rutile at 600 °C, while in Raman spectrum (Fig. S8), modes due to rutile phase are not observed in presence of anatase because of its poor scattering efficiency. Similarly, a Raman profile of other pure oxide, NiO was recorded and shows a characteristic broad band at ~500 cm^{-1} in Fig. S8 [43]. This band originates due to the strong phonon-magnon interaction at nanoparticles surface or some defects, which compete with the magnetic ordering of the nanoparticles [43]. Raman modes of another highly crystalline compound $NiTiO_3$ are marked as * in Fig. S8 appearing at 192, 230, 247, 291, 345, 395, 465, 614, 707 and 757 cm^{-1} [44]. The ten Raman active modes are assigned considering the C_{3i}^2 symmetry and $R\bar{3}$ space group of rhombohedral $NiTiO_3$ powders. The bands are sharp and intense confirming the highly crystalline nature of $NiTiO_3$ phase obtained as a result of solid state route calcined at 1000 °C. These were compared with Raman spectra of composite oxides, NTC36 and NTC11. It was observed that characteristic peaks of anatase phase were present in NTC36 and NTC11 composites along with weak peaks of $NiTiO_3$ phase in agreement with XRD results. However, the most intense mode of $NiTiO_3$ which appeared at 707 cm^{-1} was not observed in NTC11 but was present in NTC36. Signature peaks due to NiO or rutile were not observed in Raman spectra of composites due to poor scattering efficiencies of the phase.

Diffuse reflectance spectrum of white TiO_2 is compared with coloured composite oxides in Fig. 2. Here, like coloured oxides have shown similar absorption spectra. The two composite oxides, NTC11 and NTC36 show disparity in their colours. NTC11 is green colored, however, NTC36 is bright yellow, similar to NTOsg and NTOss oxides. Excluding TiO_2 (band gap ~3.2 eV), spectra of all other samples shows extended absorption in visible light; along with this a noticeable shift in absorption edge towards higher wavelengths was also observed. Band gap of all samples is calculated considering Ti edge tabulated in Table-S3 of Supplementary information. Band gap of black coloured, NiO is 3.6 eV yet; it shows absorption in visible region because of presence of vacant *3d* states of Ni above valence band which extends the photoresponse in visible region. DRS of NTC11 appears to be an overlap of absorption spectra of both NiO and TiO_2. The DRS spectra shown in curves b, d, e corresponding to NTC36, NTOsg and NTOss, respectively

are similar in nature and sample colour. The peaks at 374, 450, 743 nm and shoulder at 511 nm appearing in these spectra are characteristic peaks of $NiTiO_3$ phase and are prominent for nickel titanate, NTOsg and NTOss. 374 nm attributed to the $O^{2-} \rightarrow Ti^{4+}$ charge transfer interaction. Ni^{2+} $3d^8$ band situates between conduction band formed due to $3d$ orbitals of Ti^{4+} and valence band formed due to oxygen $2p$ orbitals [45]. Hence, charge transfer transition $Ni^{2+} \rightarrow Ti^{4+}$ occurs at lower energy compared to $O^{2-} \rightarrow Ti^{4+}$ charge transfer transition. 450 and 511 nm due to the crystal field splitting of $3d^8$ band of Ni^{2+} ions into two sub-bands called the $Ni^{2+} \rightarrow Ti^{4+}$ charge transfer (CT) bands. It also shows absorbance at 743 nm as indicated by its yellow colour [46]. NiO and $NiTiO_3$ phases were simulated by DFT using VASP software to understand the contribution of valence orbitals of different atoms in valence band and conduction band and to explain the observed absorption properties. DRS of NTC11 and NTC36 samples was also recorded after use in photocatalytic activity tests as shown in curves g and h respectively, revealed that light absorption properties of composites, were unaltered after irradiation and therefore can be reused.

Photoluminescence (PL) spectra of Ni/Ti oxides are shown in Fig. 3, reveals the course of electron and hole produced after absorption of light. From PL data, TiO_2 shows a broad emission peak in range of 355 to 530 nm with maximum peak at 427 nm recorded at excitation wavelength of 285 nm (Fig. 3a). This is related to band edge emission and shoulder at 448 nm is associated with defect/trap emission in TiO_2

[47–49]. Peak intensity is found to decrease in all oxides containing Ni ions. Ni acts as a quenching agent. PL spectra of composites NTC11 and NTC36 differ in both peak positions and profiles also. In case of NTC11, there is a broad peak (355–530 nm) with peak maximum at 427 nm corresponding to band edge emission of TiO_2, followed by weak emissions coinciding with NiO peaks. However, unlike NTC11, the PL profile of NTC36 matches with $NiTiO_3$. $NiTiO_3$ shows a broad emission same as TiO_2 but with a peak maximum shifted from 427 nm to lower wavelength of 412 nm. The peaks at 412 nm and 553 nm were observed in NTC36, NTOsg and NTOss (marked in Fig. 3a). In cases of NTC36, NTOsg and NTOss, the half widths at maximum intensity are less than that of TiO_2 or NTC11. NiO shows very poor luminescence at 450, 532, 644 and 666 nm upon photo-excitation at 365 nm as shown in Fig. 3a. Maximum activity of NTC11 for production of H_2 is related to broad range of absorption/emission from UV to visible. Preparation route has affected the PL intensity. NTO prepared by sol-gel route has shown intense emission as compared to solid state route prepared oxide. The PL signals attenuate with increasing calcination temperature for both types of $NiTiO_3$, in good agreement with literature reports [49]. It is also reported that the light absorption also decreases distinctly with increasing calcination temperature. Therefore, it is difficult to reveal the intrinsic change of photoluminescence signals with sintering.

Photoluminescence decay curves of Ni/Ti oxides upto 110 ns are shown in Fig. 3b. Excitation and emission wavelengths for all samples
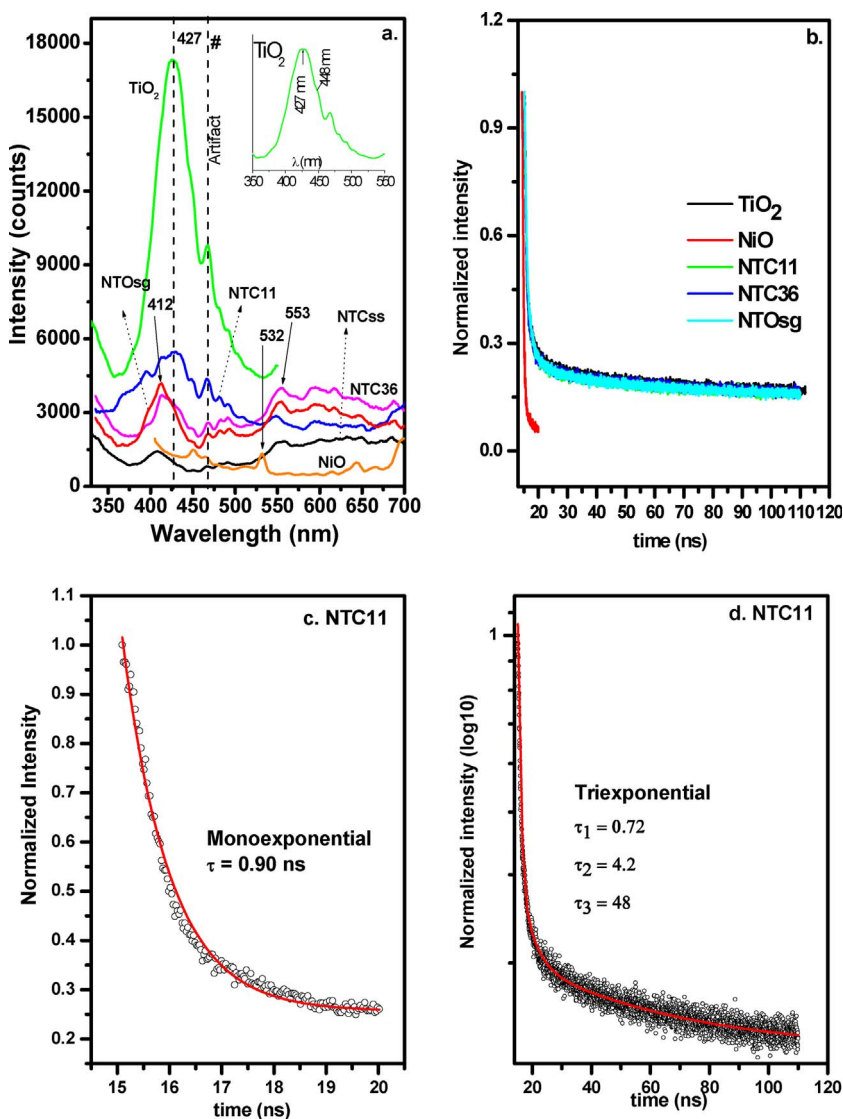

Fig. 3. a. Photoluminescence spectra of different Ni-Ti oxides b. Luminescence decay curves of TiO_2, NiO, NTC11, NTC36, NTOsg upto 110 ns. c. Mono-exponential fitting to data of NTC11 up to 20 ns and d. Tri-exponential fitting to data of NTC11 up to 110 ns.
*Artefact: instrumental peak due to lamp change at 467 nm.

Table 1
Parameters derived from fitting of decay profile (upto 110 ns) of different samples using tri-exponential decay equation.

Parameters	Samples				
	TiO$_2$	NTC11	NTC36	NTOsg	NiO
τ_1 (ns)	0.91	0.72	0.72	0.86	0.5
τ_2 (ns)	5.2	4.2	5.0	4.2	1.0
τ_3 (ns)	39	48	59	47	11
X^2 (goodness of fitting)	0.986	0.989	0.989	0.990	0.985

except NiO were monitored at 267 nm and 427 nm, respectively. NiO was excited using 339 nm to yield emission at 532 nm. Decay is much faster for NiO as compared to others. It is because Ni d^8 electrons are paramagnetic and also NiO is antiferromagnetic [50], which quenched luminescence. Decay profile of all samples apart from NiO is shown in Fig. S9a of Supplementary information upto 20 ns. Here, decay data is shown upto 20 ns because about 75% of decay is completed within 20 ns. Data are fitted with mono-exponential equation. Typical mono-exponential fitting to data of NTC11, TiO$_2$ and NTOsg are shown in Figs. 3c, S9b and c of Supplementary information, respectively. Lifetimes of 0.91, 0.90, 0.92, 1.02 and 0.68 ns were observed for TiO$_2$, NTC11, NTC36, NTOsg and NiO, respectively. NiO gives least value of lifetime among them. Lifetime values of other samples are almost unchanged within error bar of 0.10 ns. 75% decay takes place within 20 ns, beyond that (25% decay data) upto 110 ns was fitted with tri-exponential equation. Triexponential fitting of NTC11, TiO$_2$ and NTOsg is shown in Figs. 3d, S9d and e of Supplementary information respectively. Their fitting parameters are given in Table 1. The shortest lifetime ($\tau_1 < 1$ ns) is related to the band-band edge e$^-$/h$^+$ recombinations [48]. The medium lifetime ($\tau_2 = 4$–5 ns) will be related to the presence of self-trap below conduction or Ti-O charge transfer in TiO$_6$ unit. The longer component (τ_3) in lifetime (> 39 ns) will be related to oxygen defects in particles. The τ_1 contributed about 75% and remaining two components (τ_2, τ_3) contributed about 14% of decay data. τ_2 has about 98%, whereas τ_3 has 2% contribution in 14% of decay data. The value in longer component increases from TiO$_2$ to NTC11 or NTC36 or NTOsg. Except longer component in lifetime, shortest and medium components could not be distinguished significantly. It is quite obvious that photogenerated e$^-$ recombines with h$^+$ instantaneously at all three sites (τ_1, τ_2, and τ_3) of NiO as compared to other samples. This implies coexistence of TiO$_2$ with NiO in any form has helped in delaying the recombination reaction considerably.

FESEM micrographs along with EDX patterns and backscattered images for composite samples, NTC11 and NTC36 are shown in Fig. S10 of Supplementary information. FESEM images reveal agglomerates, inside which shape and dimensions of particles can be deciphered. Upon comparing figures it can be noticed that size of the particles in sample NTC11 is more homogeneous as compared to NTC36. From these images, however, it is difficult to distinguish NiO from TiO$_2$ as all particles exhibits are of similar morphology with particle size varying in the range of ~15–20 nm. Distinctly large nearly spherical particles of nearly 50 nm size were observed in NTC36 (highlighted by red outline in Fig. S10c–d. The XRD results and crystallite sizes of individual phases estimated by Scherrer equation, listed in Table-S1 suggests the emergence of highly sintered NiTiO$_3$ as secondary phase under the stated experimental conditions. This phase is more dominant in the NTC36 composite sample as compared to NTC11. Thus, large particles prominently present in NTC36 (outlined in red) are possibly belonging to NiTiO$_3$ phase. However, FESEM images of NTC11 are devoid of such large particles. It is known that large particles of NiTiO$_3$ with poor surface areas and porosity are produced by conventional synthetic routes, due to inherent problems such as high reaction temperature and heterogeneous solid phase reactions [31,39 and 40]. Lopes et al. [44] reported characterization of NiTiO$_3$ powders prepared by polymeric

precursor method after thermal treatment at different temperatures for 2 h in air atmosphere and investigations by SEM, revealed that the NiTiO$_3$ powders, heat treated between 600 °C and 1000 °C, present a mean distribution of the particle in the range of 94–306 nm. Back-scattered electrons (BSE) from NTC11 and NTC36 samples were imaged and are shown in Fig. S10e–f, respectively. BSE are used to detect contrast between areas with different chemical compositions thus can provide information of distribution of different phases. Apparently, NTC11 have shown almost uniform distribution of individual phases present in the sample in concurrence with TEM images. Thus, it appears that NiO and TiO$_2$ are uniformly distributed in NTC11 without segregation of either phase. NiO and TiO$_2$ may not be distinguished by BSE due to similar molecular weight. However, backscattered image of NTC36 shows prominence of two phases represented by bright and dark field. EDX patterns show that intensity of peaks due to Ni relative to Ti increases from NTC36 to NTC11 (Fig. S10g–h). Bulk composition was determined by EDX and ICPOES and was in agreement within experimental error (± 5%) with the calculated values for both the composites in Table-S4 of Supplementary information.

Low and high resolution TEM images with particle size distribution and SAED patterns are shown in Fig. 4a and b for NTC11 and NTC36, respectively. Low resolution image shows agglomeration of particles. Faceted particles with proper boundaries could be resolved within agglomerates. HR-TEM images reveal that the material is highly crystalline, as depicted by well defined lattice fringes. A high resolution image of NTC11 reveals lattice fringes with fringe width of 0.35 nm and 0.32 nm belonging to *101* plane of anatase and *110* plane of rutile phase of TiO$_2$, respectively. Particle size observed from TEM data was similar to the crystallite size obtained from XRD which reveals that each grain corresponds to single crystallite [51]. Particle size distribution (PSD) derived from low resolution image of NTC11 (Fig. 4a) suggests maximum number of particles falls in range of 10–30 nm, while distribution shifts towards higher particle size in NTC36 (Fig. 4b) with majority of particles more than 30 nm in size. Unlike NTC36, NTC11 comprises of very small particles also, say 5–10 nm and is devoid of very large particles of 50–55 nm. HR-TEM of NTC36 nanoparticles (Fig. 4b) shows lattice fringes with d-spacing of 0.35, 0.27 nm and 0.24 nm which corresponds to *101* plane of anatase, *104* plane of NiTiO$_3$, *111* plane of NiO phase, respectively. Diffused rings with dotted pattern forms SAED of NTC11 and NTC36 revealing nanocrystalline nature of these powders. These patterns were indexed and found to consist of phases in agreement with XRD results. HAADF – STEM images of NTC11 were recorded at low and high magnification (Fig. 4c(i–iv)). Bright and dark contrast in HAADF image arises due to difference in average atomic number corresponds to TiO$_2$ and NiO, respectively. Electron energy loss spectroscopy (EELS) at selected positions from adjacent particles showed presence of peaks due to Ti and Ni, respectively (Fig. 4cii). The chemical identification using EELS suggested that NiO and TiO$_2$ are in close proximity to each other (c iii–c iv).

XPS survey spectrum indicates presence of Ni, Ti, O and C elements with photoelectron peaks appearing at binding energies 853(Ni $2p_{3/2}$), 872(Ni $2p_{1/2}$), 529(O $1s$), 458 (Ti $2p_{3/2}$), 464 (Ti $2p_{1/2}$) and 285 eV (C $1s$). Typical binding energy values observed for different elements are tabulated in Table-S5. Fig. 5a shows high resolution XPS spectra of Ni ions present in different samples. The XPS spectrum of NiO is quite complex and is deconvuluted to yield peaks at 853.81, 855.78, 860.92 eV in the Ni $2p_{3/2}$ region (Fig. 5b) and 872.8 and 879.63 eV for Ni $2p_{1/2}$ region. The first two peaks at 853.81, 855.78 eV are attributed to multiplet splitting of Ni $2p_{3/2}$ [52], 860.92 and 879.63 eV are satellite peaks of Ni $2p_{3/2}$ and Ni $2p_{1/2}$ respectively. The broadening of the main line and the satellite is due to interactions of the central Ni atom with either neighbouring NiO$_6$ octahedra or with oxygen-deficient defects [53]. The deconvuluted Ni $2p$ XPS spectrum of composite oxides NTC36 and NTC11 is shown in Fig. 5c and d respectively, to reveal the multiple peaks due to Ni^{2+}, at positions observed for free NiO. The spectrum confirmed the existence of NiO with Ni at + 2 oxidation state
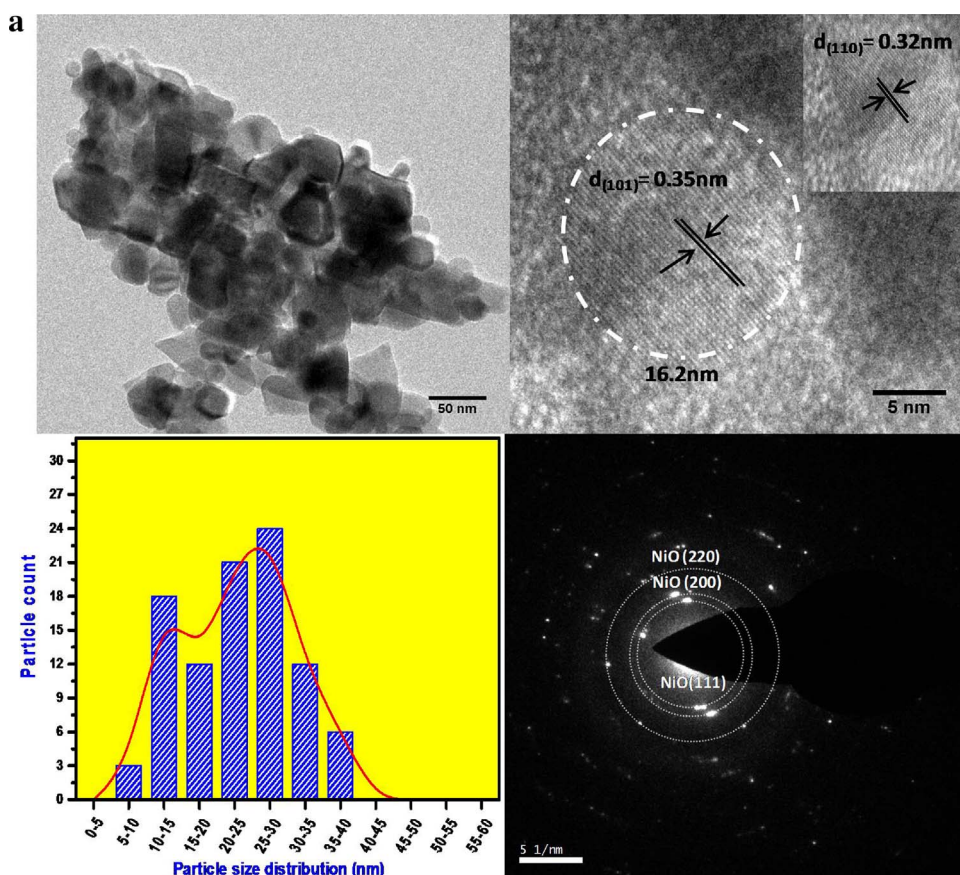
Fig. 4. TEM, HR-TEM images, SAED pattern and particle size distribution are shown in clockwise direction for (a) NTC11 (b) NTC36 and (c) low (i) and high (iii–iv) magnification STEM-HAADF images of the NTC11 sample along with EELS (ii) of the selected area indicated as positions 1 and 2. Bright and dark contrast in HAADF image arising due to difference in average atomic number corresponds to TiO_2 and NiO respectively.

in composite samples. However, for the NTC11, the first multiplet appears with lower intensity as compared to free NiO. The homogeneous distribution of TiO_2 molecules around NiO in NTC11 has probably affected the mutiplet intensity of Ni 2p. This suggests the co-existence of NiO and TiO_2 in composite material, NTC11. In case of nickel titanate, NTOsg, comparatively a sharp peak at 856.01 eV was observed corresponding to symmetric octahedral environment around Ni ions situated in cubic unit cell of $NiTiO_3$. The oxidation state of Ni and Ti ions in used NTC11 sample were same as fresh sample, confirming the chemical stability of the composite oxides after photocatalytic activity tests. Ni/Ti ratio is maintained, however, O/M ratio has increased due to adsorption of water molecules, affecting the multiplet intensity (Fig. 5d–e).

BE values in the range of 455.1 to 461.0 and 461.0 to 467.2 eV (Fig. 6a) for Ti $2p_{3/2}$ and $2p_{1/2}$ respectively, in the range of 526.9–537 eV (Fig. 6b) for O1s and from 281.15–287.6 eV (Fig. S11 of Supplementary information) for C1s core levels for TiO_2, NiO, NTC11 and fresh and used NTC11 can be seen. These values confirm that Ti is in the +4 state in both TiO_2 and Ni-Ti oxides [54]. Ti 2p XPS spectrum was deconvulated to reveal the contribution of Ti^{4+} ions from different phases as shown in Fig. 6a. Ti 2p peak shifts by 0.67 eV on crystallization into $NiTiO_3$ (NTOsg) phase (Fig. 6a) as compared to anatase TiO_2 attributed to different local environment experienced by Ti ions in $NiTiO_3$ lattice [55]. As obvious, the intensity of Ti 2p XPS signal decreased in NTC11 as compared to NTC36 in accordance with the proportion of Ti content present in each sample. As explained above the expected bulk composition of composite oxides, NTC11 and NTC36 were found to be in agreement with the experimental values analysed using ICP-OES results (Table-S4). However, the elemental composition on surface of individual photocatalysts was derived from XPS (Table 2). The surface concentration of [Ni]/[Ti] was 0.24 in NTC36, lower than the ideal value 0.54. While, it was found to be 0.95 in case of NTC11 which is in close agreement with the expected value of 1.0. This

suggests that surface of NTC36 unlike bulk, is rich in Ti and deficient of Ni ions. For, NTC11, the composite character of bulk is extended upto surface and Ni and Ti metal ions are homogeneously distributed over the surface of NTC11. This explains how the multiplicity of Ni 2p spectrum is affected in NTC11. Thus, XPS investigations revealed that surface properties of NTC11 composite oxide are more favourable for the photocatalytic activity as compared to NTC36. The metal ions act as active sites for adsorption of water molecules. For, used NTC11 oxide the ratio is same as fresh sample within experimental error, suggesting that surface composition after photoactivity tests has not varied. Thus, leaching of the Ni or Ti metal ions from the surface of the photocatalyst did not occur during the activity evaluation. O1s peak obtained from pristine TiO_2, NiO as well as Ni-Ti oxides could be resolved mainly in two spectra using a gaussian fit as shown in Fig. 6b to yield a major peak at ~529 eV and another one at ~531 eV. The secondary peak was assigned to $-OH^-$ (hydroxy) species present on the surface in addition to bulk oxide (O^{2-}) species [54]. In case of NiO, the broad O1s peak is resolved in three peaks at 529.22, 531.06 and 534.01 eV. The additional peak at 534.01 eV observed in NiO spectrum is arising from chemisorbed oxygen containing species from either water, oxygen, CO or CO_2 [56]. The surface concentration of [O]/[Ti] in pristine TiO_2 from Table-2 exceeds the ideal value of 2 and in case of NiO also, it is ~4 ideally should have been 1. Thus, indicating that surface is rich in oxygen which can be explained by presence of adsorbed hydroxy species in the form of $Ti(OH)_4$ linkages where required [O]/[Ti] is 4 on surface of TiO_2. Presence of additional chemisorbed oxygen on surface of NiO explains the exceptionally high observed [O]/[Ni] ratio. Further, increase in [O]/[M] (where M = Ni + Ti) concentration of used NTC11 sample indicated that Ni-Ti-O oxides offers more active sites for adsorption of water molecules.

Photocatalytic activities of *pn* semiconductors, NTC36 and NTC11 was evaluated under different sources of light (Figs. 7–11) and compared with individual oxides, NiO, TiO_2 and $NiTiO_3$. 100 mg of
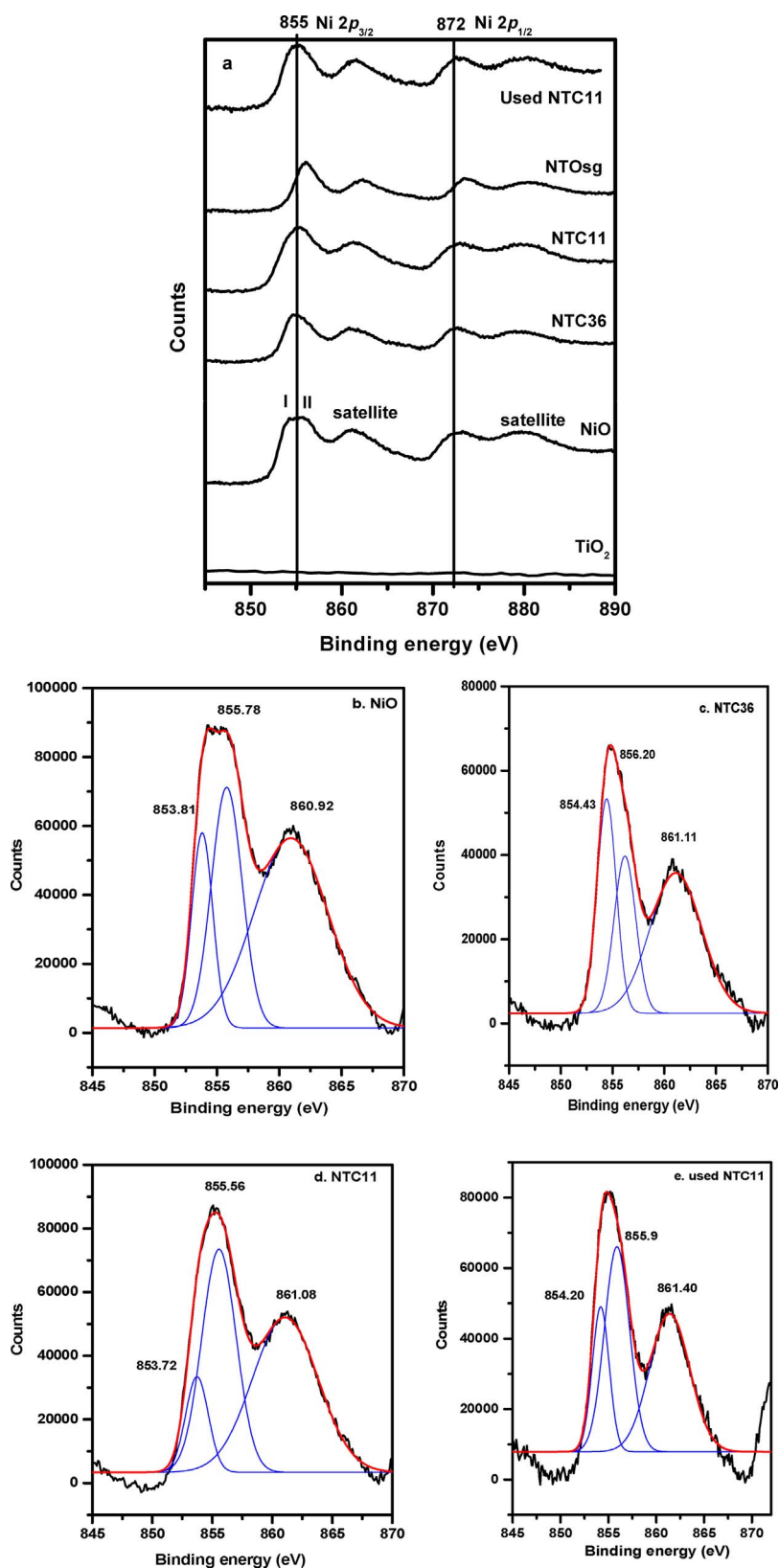
Fig. 5. a. Overlay of XPS spectra corresponding to Ni $2p_{3/2}$ and Ni $2p_{1/2}$ lines for different samples. Deconvulation of Ni $2p_{3/2}$ peak in b. NiO c. NTC36 d. NTC11 and e. used NTC11. [I] and [II] are multiplets due to Ni $2p_{3/2}$.

photocatalyst was suspended in a mixture of water and methanol (2:1 v/v), irradiated in sunlight, UV–vis and exclusively visible light source under evacuated conditions. H$_2$ yield, AQE, SFE achieved over different samples under different light sources and conditions is tabulated in Table-S6. Figs. 7 and 8 show hydrogen yield in μmol obtained over Ni-Ti oxides in sunlight and medium pressure mercury light source

with UV–vis photoemission, respectively. Hydrogen yield increased linearly with irradiation time. No evolution of hydrogen gas was detected in dark. Also evolution of H$_2$ bubbles was observed in evacuated conditions under sunlight irradiation [4]. Evacuation before irradiation is favorable to get maximum hydrogen yield [4,32]. To establish structure-activity correlations, two more Ni/Ti oxides with
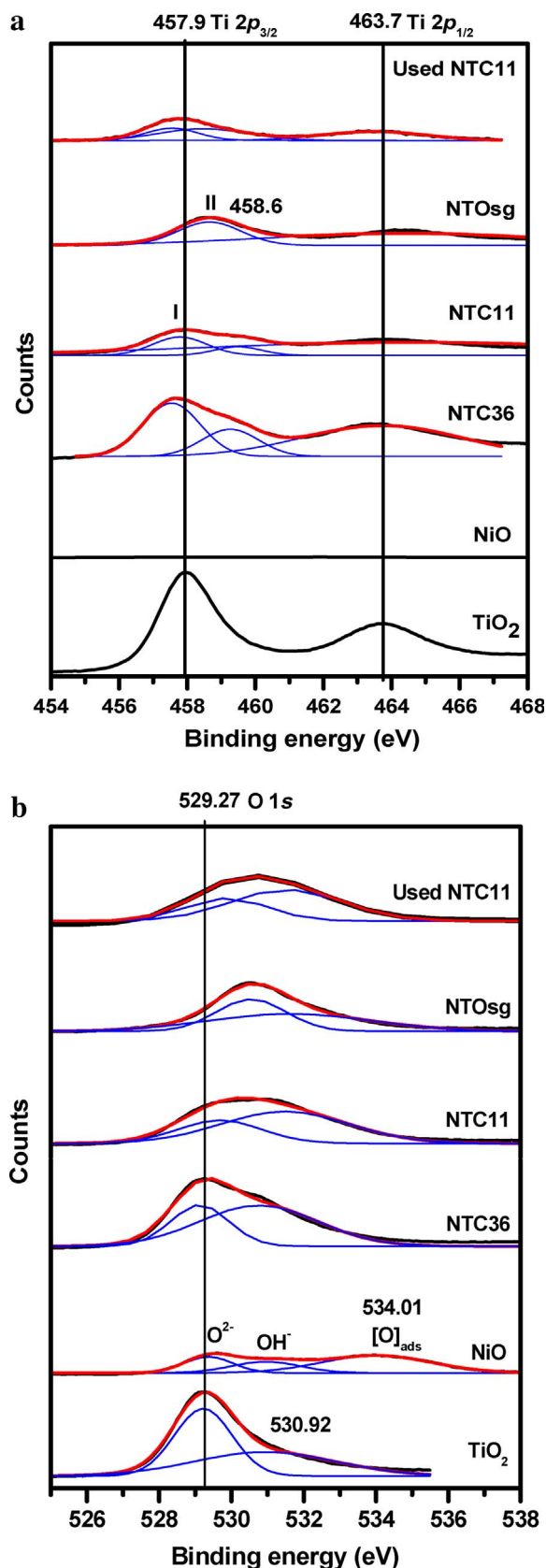
Fig. 6. Overlay of XPS spectra corresponding to a. Ti *2p* and b. O *1s* lines for different samples. Broad peaks were deconvulated to relatively quantify various oxidation states of an element present in a sample. [I] Anatase and [II] NiTiO$_3$.

Table 2
Elemental compositions derived from XPS study of fresh and used composite Ni-Ti oxides.

Sample	Chemical composition (atom%)				
	Ti	Ni	O	[Ni]/[Ti]	[O]/[M] M = Ti + Ni
TiO$_2$	24.8	–	75.2	–	3.0
NiO	–	19.92	80.08	–	4.02
NTC36	20.67	5.05	74.27	0.24	2.9
NTC11	11.15	10.61	78.24	0.95	3.6
NTO sg	13.70	7.60	78.70	0.55	3.7
NTC11 used	10.20	9.80	80.0	0.96	4.0

compositions NiO:TiO$_2$ (0.65:0.35), abbreviated as NTC63 and other is NiO:TiO$_2$ (0.15:0.85), abbreviated as NTC18 were evaluated and compared with other compositions under UV–vis irradiation and sunlight. NTC18 shows presence of predominatly anatase along with minor NiO, NiTiO$_3$ and rutile phases and whereas NTC63 shows NiO as major phase with NiTiO$_3$ in substantial amounts, while anatase is in minor phase with insignificant amount of rutile as revealed by the XRD patterns (Fig.S12 of the Supplementary information). Both were found to be less active as compared to most active NTC11 composite. The decreasing order of photocatalytic activity of samples calcined at 600 °C in sunlight is as follows: NTC11 (H$_2$ @ 20.4 µmol/h) > NTC18 (H$_2$ @ 5.17 µmol/h) ~ TiO$_2$ (H$_2$ @ 2.5 µmol/h) ~ NTC36 (H$_2$ @ 2.34 µmol/h) > NTOsg (H$_2$ @ 1.52 µmol/h) > NTC63 (H$_2$ @ 1.36 µmol/h) > NTOss (H$_2$ @ 0.22 µmol/h) and under UV–vis illumination is as follows: NTC11 (H$_2$ @ 84 µmol/h) > NTC18 (H$_2$ @ 51.28 µmol/h) > TiO$_2$ (H$_2$ @ 29.1 µmol/h) ~ NTC36 (H$_2$ @ 24.5 µmol/h) > NTOsg (H$_2$ @ 10 µmol/h) > NTOss (H$_2$ @ 1.8 µmol/h) > NTC63 (H$_2$ @ 0.88 µmol/h) > NiO (H$_2$ @ 0.4 µmol/h), respectively. The trend shows that composite, NTC18 consisting of higher proportion of TiO$_2$ has performed reasonably well, with activity higher than parent TiO$_2$, but lower than NTC11. However, NiO rich composite, NTC63 has shown NiO like poor activity. Thus, both composites, NTC63 and NTC18 have shown performance, corresponding to the predominant phase. The poor activity of NTC36 is attributed to presence of derogatory, NiTiO$_3$ phase in dominance in this sample. Thus, ideal composition for exploiting the role of *pn* junctions is 1:1 in present study. Similarly, Parida et al. [57] investigated NiO/Ta$_2$O$_5$ composites with varying molar ratio of both the oxides and it was found that 1:3 was most active due to formation of *pn* junctions and minimum hindrance from the secondary phase, NiTa$_2$O$_6$ developed.

Composite NTC11 has performed considerably better than individual pure oxides such as nickel titanate and nickel oxide under different light sources. However, photocatalytic activity of NTC36 is poor than TiO$_2$. Among all these samples, maximum photocatalytic activity was observed for NTC11 with H$_2$ generation rate of 204 µmol/h/g and 840 µmol/h/g of hydrogen yield with apparent quantum efficiency 2% and 5.3% in sunlight and UV–vis irradiation, respectively. To enhance the hydrogen yield, 1% (w/w) Pt was loaded as co-catalyst over NTC11 by photodeposition method. Pt provides sites for H$^+$ reduction by photogenerated electrons trapped due to schottky barrier. Pt (1% w/w)/NTC11 photocatalyst liberated H$_2$ @ 537 µmol/g/h (Fig. 7) with AQE of 5.4% under sunlight irradiation and 1250 µmol/g/h (Fig. 8) with AQE of 7.8% (Table-S6) under UV–vis light irradiation. Stability of composite photocatalysts NTC11 and Pt/NTC11 was also established under sunlight for 60 h over same 100 mg of sample (Fig. 9). Linear H$_2$ evolution was observed over Pt/NTC11 upto 60 h under sunlight at an average rate of 490 µmol/g/h with standard deviation of (+/− 2.7%). Sustained H$_2$ evolution without any deterioration in photocatalytic activity was found for 60 h. Methanol which was initially added, sufficed for the complete activity test of 60 h. So, intermittent addition of sacrificial agent was not required. Further, to establish the visible light activity exclusively, the performance of NTC11 was also evaluated for 35 h under visible light lamp with λ$_{max}$ at
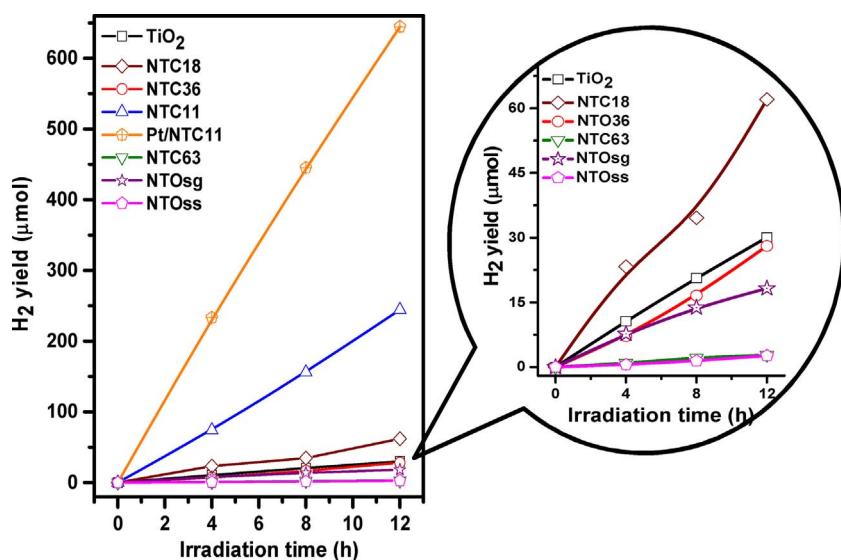
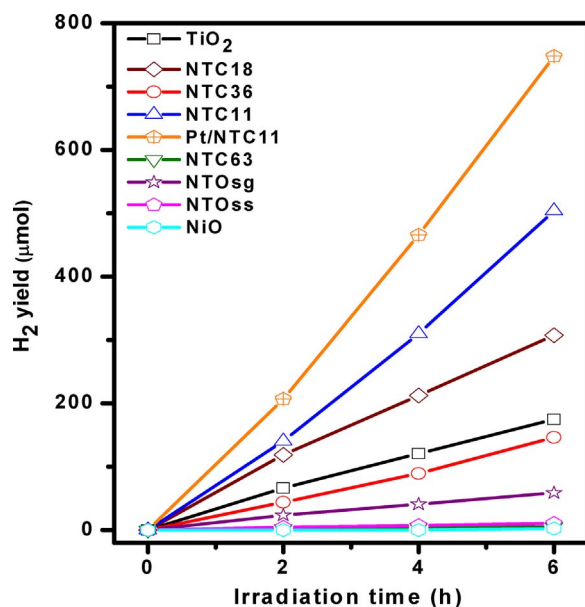Fig. 7. H$_2$ yield monitored over different Ni-Ti oxides under sunlight carried out during 10:00–16:00 h IST.

Fig. 8. Time courses of photocatalytic H$_2$ generated over Ni-Ti-O oxide composites under UV–Vis irradiation.
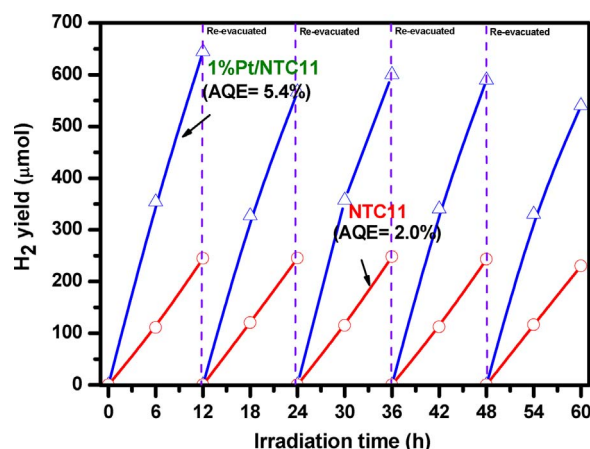

Fig. 9. Recyclability of photocatalytic H$_2$ generation over NTC11 and Pt/NTC11 evaluated for 60 h by irradiating the sample under sunlight.
Experimental conditions: 100 mg of photocatalyst was suspended in water + methanol (33% v/v), evacuated and illuminated under sunlight for duration of 6 h in a day during afternoon (10.00–16.00 IST) and H$_2$ yield was monitored for 10 days with intermittent evacuation after 12 h of irradiation.

536 nm without UV emission (Fig.S3 of Supplementary information). H$_2$ evolution @ 306 μmol/g/h with AQE of 1.6% was constantly observed for 35 h over NTC11 (Fig. 10) under visible light. Thus, visible light activity and stability of NTC11 is established under both sunlight and visible light illumination. XPS results, have established that the *pn* composites retain the chemical and compositional stability on surface after photocatalytic reduction of water to H$_2$.

Calcination temperature and phase compositions were very critical and found to determine the overall hydrogen yield. Photocatalytic activities of all the samples prepared with varying heat treatment discussed above (XRD of samples are shown in Fig.S6 of Supplementary information) were evaluated and shown in Fig. 11 to establish structure-activity correlations. The decreasing trend in activity was NTC11-LT 600 °C, 10 h > NTC11-LT 600 °C, 3 h > NTC11-HT 600 °C, 10 h > NTC11-LT 500 °C, 5 h. The fall in activity coincides with the appearance of NiTiO$_3$ phase. To verify the results, a sample of NiTiO$_3$, synthesized by solid state was tested and found to result in poor photocatalytic H$_2$ yield @ of 2.2 and 18.0 μmol/g/h in sunlight and UV–vis light irradiation, respectively (Figs. 7 and 8). NiTiO$_3$ phase has shown

lowest activity among all Ni-Ti oxides under investigation in all conditions. Low activity of NTC11-LT calcined at 500 °C is attributed to poor crystallinity of anatase TiO$_2$ and cubic NiO phases present in sample (Fig.S6a) as compared to the 600 °C calcined sample. From the trend, it is observed that activity increases with increase in crystallinity of the NiO and TiO$_2$ phases. Thus, both crystallinity and presence of NiTiO$_3$ phase determined the overall H$_2$ yield. Among all samples maximum photocatalytic hydrogen yield was observed over NTC11 or NiO-TiO$_2$ (1:1) – LT calcined at 600 °C for 10 h with H$_2$ yield @ 204 μmol/g/h under sunlight (Fig.S6c) persistent upto 60 h. Presence of NiTiO$_3$ phase is minimal in NTC11, and therefore resulted in maximum activity in line with our other results. Thus, gel drying temperature of 90 °C and calcination at 600 °C for 10 h are the optimized conditions that offer a well crystalline *pn* nanojunction comprised of NiO and anatase TiO$_2$ phases (1:1) with minimal amount of NiTiO$_3$.

5. DFT

It was important to understand the electronic properties and band structure of individual oxides constituting the composites. The electronic properties of TiO$_2$ are well studied where distorted tetragonal
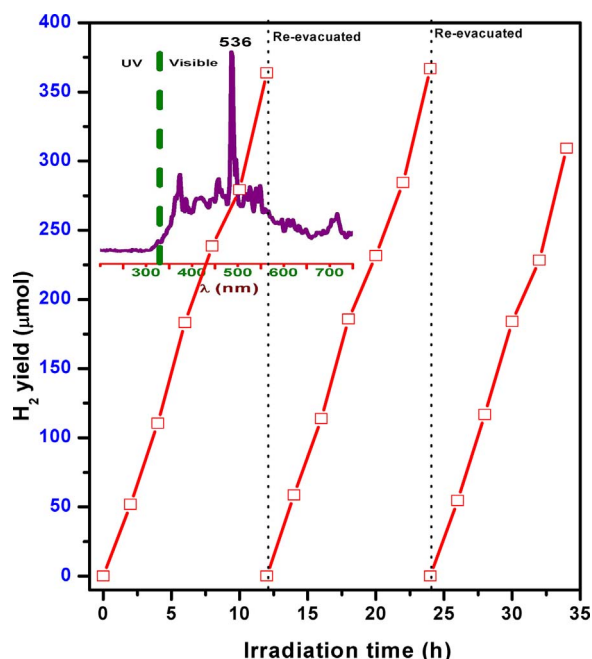
Fig. 10. Visible light activity of NTC11 was established by monitoring H_2 yield for 35 h under medium pressure mercury lamp emitting wavelengths longer than 400 nm (λ_{max} = 536 nm). Emission spectrum is shown in inset.
Experimental conditions: 100 mg of photocatalyst was suspended in water + methanol (33% v/v), evacuated and illuminated under visible light source for 35 h with intermittent evacuation at regular intervals.
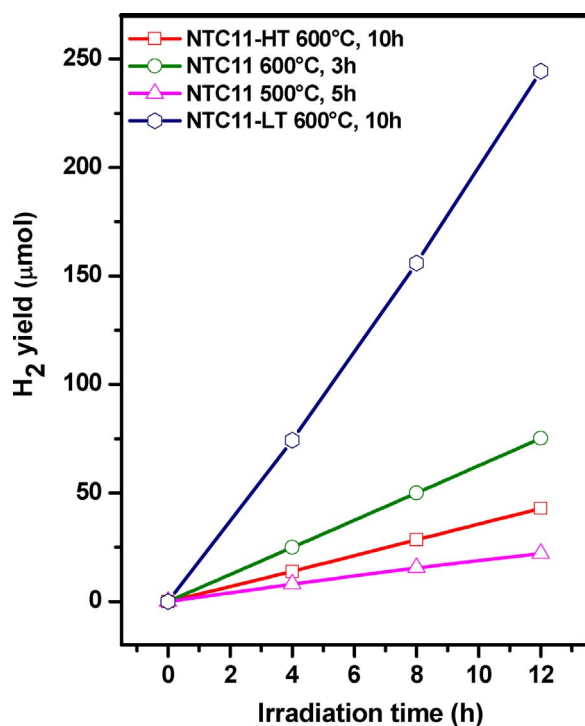

Fig. 11. Effect of calcination temperature and crystallinity on photocatalytic properties was investigated by evaluating photocatalytic H_2 yield over a NiO and TiO_2 composite in 1:1 composition synthesized under varying heat treatment conditions corresponding to samples shown in Fig. S6 of Supplementary information.

lattice imparts favourable photocatalytic properties to anatase TiO_2 [58]. In our earlier work [32,33] we have theoretically emphasized better photocatalytic properties of n-TCO oxides such as indium titanate as compared to n-TiO_2. First principles DFT based band structure

calculations were performed on single phase rhombohedral, $NiTiO_3$ and reported elsewhere by us [31] which revealed that strong intermixing of Ni -$3d$ with O -$2p$ orbitals occurred in the valence band of $NiTiO_3$ and resulted in generation of a pseudo band gap at 1.36 eV. This pseudo band gap might act as hindrance and may contribute in weakening the intensity of electronic transition due to $Ni^{2+} \rightarrow Ti^{4+}$ charge transfer. The highlights of these calculations are mentioned in Supplementary information, S1.

Since NiO shows spin polarized calculations, the electronic structure of NiO was calculated using VASP code in order to clarify the distribution of valence states of Ni, O atoms near Fermi level and to understand the role of NiO in modifying the photocatalytic properties and enhancing the visible light activity of *pn* nanocomposites withTiO_2. Fig. 12a show calculated band structures of NiO along a few high-symmetry directions; while Fig. 12b show total as well as site- and *l-projected* partial density of states (DOS) for NiO. The lowest unoccupied state (LUMO) are found at G-point (0, 0, 0) and X point (0, 1, 0) in the conduction band whereas the highest occupied state (HOMO) are found at point L (½, ½, ½) in the valence band as shown in Fig. 12a. The O-$2p$ states in the valence band show a sharp peak near the Fermi level representing its localized nature. The strong optical transitions are due to flat bands from valence band to conduction band (shown by arrows in Fig. 12a) and these are found along L to G point, W to X point, from G–X to G point and G–X to X point. These transitions from highest occupied (HOMO) states in valence band to the unoccupied states (LUMO) in conduction band are at different k vector and exhibit a consistent band gap of about 3.0 eV. Thus, NiO is an indirect band gap material (Fig. 12a). The calculated Eg (band gap) of 3.0 eV is not consistent with the reported optical band gap (3.6 eV) due to limitations of the calculations performed here. The Fig. 12b shows the contribution of individual orbitals of Ni and O in formation of valence band and conduction band. Positive and negative n(E) corresponds to the majority and minority spin states, respectively. This convention has been used in all other DOS plots (Fig. 12b). Since NiO- shows spin polarized calculations, net magnetic moment was found to be 2.0 Bohr magneton. Near E_f, fermi level O-$2p$ and Ni-$3d$ states dominate show strong hybridization. Ni-$4s$ states contributes in the middle region of valence band at around −3 eV where contribution from O-$2p$ states is smaller. The position of conduction band is dictated by Ni-$3d$ states. The valence band consists of mainly O-$2p$, Ni-$4s$ and $3d$ states (Fig. 12b), while the conduction band is mainly comprised of Ni-$3d$ states. The O $2p$ states contribute considerably to the Density of states near Fermi level, whereas the Ni $3d$ and $4s$ just make the contributions in lower and mid part of valence band, respectively. Band calculations on NiO reveals that the large dispersion of Ni $3d$ and $4s$ states, and the optical indirect transition are in favour of photon energy storage and electron-hole separation to benefit the photocatalytic activity of NiO-TiO_2 composites. The theoretical calculations reveal a net charge transfer of 1.248 electrons from Ni to O ions. The charge transfer properties of NiO lead to longer carrier lifetimes [59,60] facilitating e^-/h^+ separation for higher efficiencies, and its conduction band edge is suitable for driving hydrogen evolution via water splitting [61]. Nickel oxide is an inexpensive yet highly promising candidate for photocatalytic applications. NiO has a rock salt structure, with Ni^{2+} ions anti-ferromagnetically coupled in the [111] direction [62]. The valence band edge (VBE) is composed of O $2p$ and conduction band edge (CBE) of Ni $3d$ character. This makes NiO a charge-transfer (CT) material. CT materials have VBE and CBE of different characters in contrast to Mott-Hubbard type semiconductors in which the VBE and CBE both have Ni $3d$ characters [62]. The large, indirect band gap of NiO has however limited its functionality as a light absorber. In spite of absorbing light in UV region, the colour of NiO is black which is attributed to the impurity levels created above VBE and below CBE [63–66]. This model study is also useful in understanding the performance of similar photocatalysts.
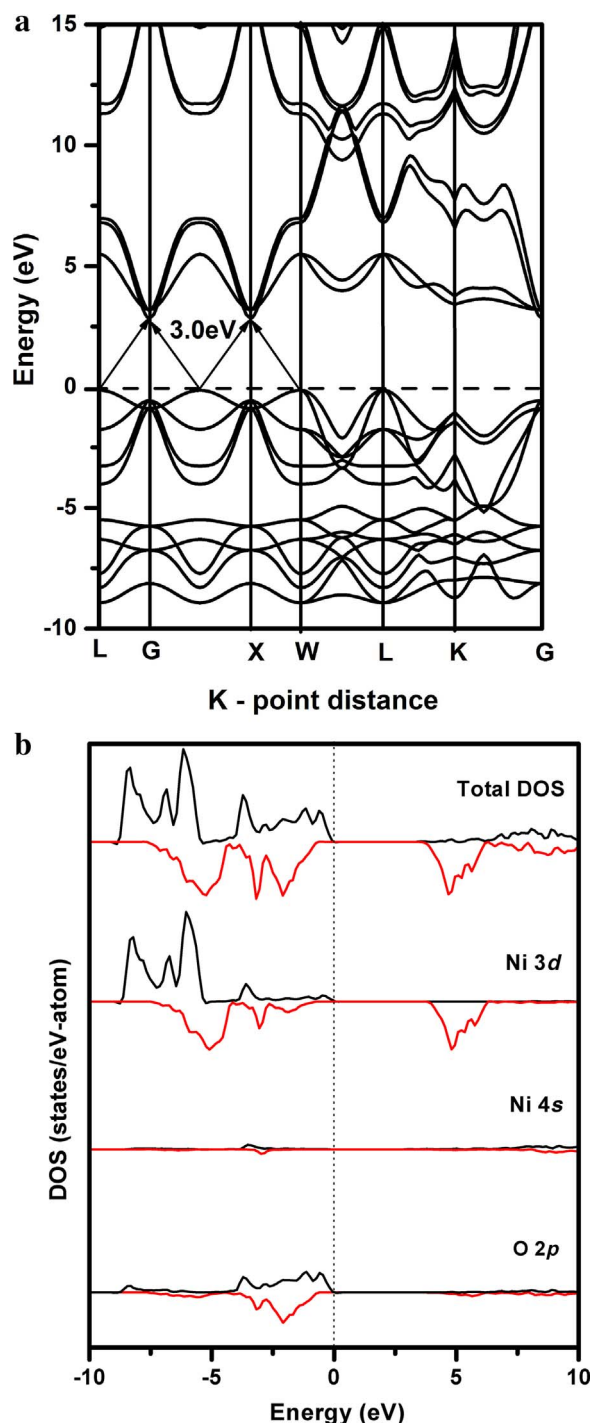
Fig. 12. a. Band structure of NiO along high-symmetry L (1/2, 1/2, 1/2), G (0, 0, 0), X (0, 1, 0), W (1/2, 1, 0) and K (0, 3/4, 3/4) directions. It can be seen from band gap that there is existence of an indirect band gap of 3 eV b. Site- and angular momentum-projected partial density of states for NiO showing the valence band to be mainly composed of O -2p and Ni -3d and 4s.

6. Discussion

In the present study, authors prepared the nanocrystalline composites of NiO and TiO$_2$ oxides in two different compositions, with an objective to create the interfacial contact between diverse semiconductors; p and n type so that electric field is induced within catalysts particles, leading to efficient separation of charge carriers, e^- and h^+ which are generated during the photocatalytic process. Further, to accentuate the role of pn heterojunctions in composites, the

photocatalytic properties of these composites; NTC11 and NTC36 were investigated in detail for H$_2$ evolution reaction and compared with the pure oxides, NiO, TiO$_2$ and NiTiO$_3$ prepared under identical conditions. It was found that among all samples, NTC11 was distinctly most active and repetitive cycles yielded reproducible H$_2$ yields for 60 h under sunlight confirming its photostability under prolonged exposure. Ideally, the elemental composition, Ni/Ti on surface and bulk of composite, NTC11 should be 1, here it pertains to 0.95 on surface investigated by XPS and is 0.99 in bulk, characterized by both ICP-OES and EDX suggesting that for each Ni there is one Ti in bulk, however surface of NTC11 is slightly rich in Ti. Aggregation or segregation of any phase was not observed in backscattered FESEM image of NTC11. Thus, 1:1 phase composition and almost uniform distribution of NiO and TiO$_2$ phases was verified in the composite, NTC11 prepared in the present study. Phase identification by XRD revealed the formation of desired composite where, crystalline NiO and TiO$_2$ phases appear with minimal NiTiO$_3$ phase. Raman spectra confirmed the presence of tetragonal anatase TiO$_2$ phase. FESEM images and TEM/SAED microscopy showed presence of 10–20 nm sized nano-crystalline particles. NiO has extended the light absorption properties of TiO$_2$ (Eg = 3.2 eV), by shifting absorption edge towards higher wavelengths in visible light. Unfortunately, it is difficult to determine the exact nature of Ni–Ti–O linkages/interactions on surface or bulk, but it may be assumed on the basis of above that the NiO and TiO$_2$ phases are in close proximity and it is very likely that pn junctions would commence by their interaction in the NTC11 composite. These close interactions of NiO-TiO$_2$ oxides leading to pn heterojunctions, would affect the band structure and electronic structure at the interface and consequently improves visible light absorption and photocatalytic activities of NTC11 composite. Performance of NTC11 composite as photocatalyst would be primarily determined by proper alignment of band levels of p and n semiconductors at the heterojunction. Valence band offset (ΔE_v) and conduction band offsets (ΔE_c) at NiO and TiO$_2$ heterojunction was calculated and schematically shown in Fig. 13a. $\Delta E_V = (E_{CL}^{NiO} - E_{VBM}^{NiO}) - (E_{CL}^{TiO2} - E_{VBM}^{TiO2}) - \Delta E_{CL}$; and $\Delta E_c = $ (band gap$_{TiO2}$ − band gap$_{NiO}$) − ΔE_v, where E_{CL}^{NiO} and E_{CL}^{TiO2} are observed core level energies of Ni 2$p_{3/2}$ and Ti 2$p_{3/2}$ in the XPS spectra of pure samples of NiO and TiO$_2$, respectively and ΔE_{CL} is the difference between core level energies of Ni 2$p_{3/2}$ and Ti 2$p_{3/2}$ observed in the composite, NTC11. ΔE_v and ΔE_c were found to be 0.53 eV and 0.93 eV respectively, based on detailed calculations shown in Supplementary information, S2. Since, the zero point of the binding energy scale corresponds to the Fermi level (E$_F$), the position of the E_{VBM}^{NiO} and E_{VBM}^{TiO2} (valence band maximum) with respect to E$_F$ as expected, was negative (−1.23 eV) for p type NiO and positive (2.56 eV) for n type, TiO$_2$ semiconductors. Based on these calculations, the type-II band alignment was observed in NTC11 as shown in Fig. 13a where e^- will be transferred from CB of NiO to CB of TiO$_2$ and h^+ will flow from VB of TiO$_2$ to VB of NiO purely driven by the band energetics. A pictorial representation of the most probable mechanism proposed for NTC11 is shown in Fig. 13b. The alignment of bands in this new configuration has effectively reduced the forbidden gap to 3.2-ΔE_v = 3.6-ΔE_c = 2.67 eV at the pn junctions in the composite oxide. Thus, in present study, a composite of pn oxides offers lower band gap energy of 2.67 eV with effectiveness in charge separation leading to efficient improved photocatalyst with sustainable H$_2$ yield for 60 h in sunlight. DFT studies above have shown that NiO is a charge transfer material, and as a p semiconductor at pn interface, will transfer e^- s to n semiconductor and h^+ will flow across the junction towards NiO oxide. The charge transfer properties of NiO leads to a longer carrier lifetimes facilitating e^- and h^+ separation for higher efficiencies. In support of this band alignment scheme, time resolved photoluminescence spectra have revealed increased life times of charge carriers due to efficient separation at the heterojunctions induced in NTC11. Direct evidence of delaying the e^-/ h^+ recombination at pn junction between NiO and TiO$_2$ appears from τ_1 and τ_2 derived from triexponential fitting and also from
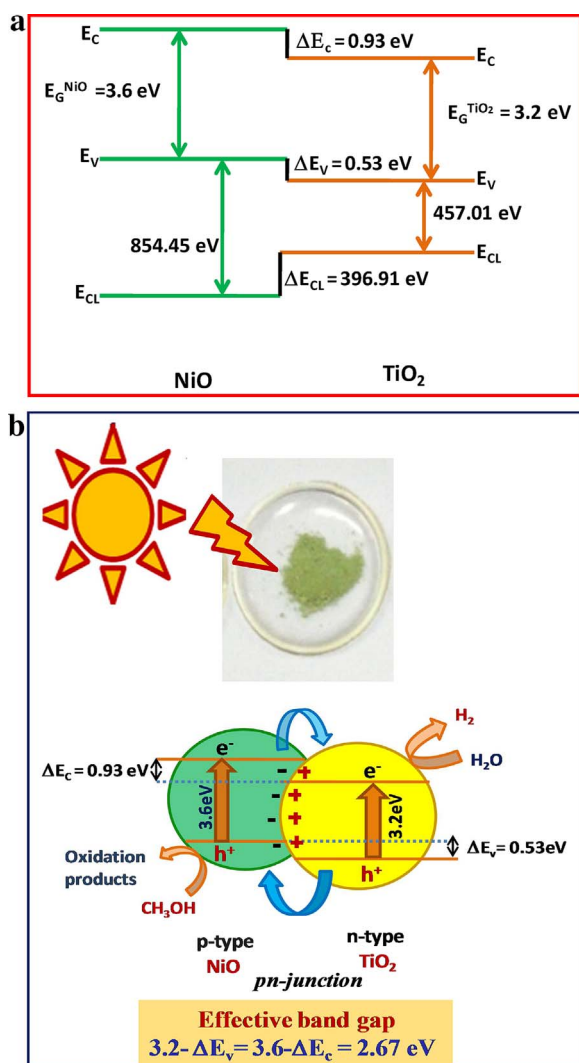
Fig. 13. a. Schematic diagram of band alignment derived at the interface of NiO-TiO$_2$ semiconductor. b. A pictorial representation of the most probable mechanism proposed for composite, NTC11.

monoexponential fit. Lifetimes of 0.91 ns in TiO$_2$ is similar to 0.90 in NTC11 suggesting that band edge recombination which is contributing to 75% decay is governed by presence of TiO$_2$ and not by NiO despite the fact that free NiO is available in equal proportion as TiO$_2$ in NTC11. Similarly, τ_2 orginating from recombination reaction at self trap states are also same as TiO$_2$. However, τ_3 is 39 ns in TiO$_2$, 48 ns and 47 ns in NTC11 and NTOsg respectively, and 59 ns in NTC36 much higher than NiO of 11 ns. By DFT calculations it was revealed that NiO is antiferromagnetic and PL quencher leading to instantaneous recombination of e^- and h^+ over pure NiO. By proportion itself and by characterization results, it is evident that free NiO is substantially present in NTC11 than NTC36. Thus, it is expected that presence of PL quencher in NTC11 composite will enhance the recombination. However, it was observed that life times τ_1, τ_2 and τ_3 has increased from 0.5 ns, 1.0 ns and 11 ns observed in pure NiO to 0.72 ns, 4.2 ns and 48 ns in composite NTC11, respectively. The increased life times and suppressed recombination rates in NTC11 can be explained by composite formation of NiO with TiO$_2$ where heterojunctions formed between *p* and *n* type semiconductors facilitates the efficient charge separation corresponding to type-II band alignment characteristics (Fig. 13). Among the NTC36 and NTC11, τ_1 and τ_2 are comparable; however, τ_3 is higher for NTC36. The recombination reaction at oxygen defects is quantified as τ_3. This implies NTC11 has more of oxygen vacancies due to multiphasic nature of

NTC11 relative to NTC36 in which NiTiO$_3$ phase predominates. The grain boundary between two phases acts as sites for e^- and h^+ recombination. Thus, more the grain boundaries higher will be the rate of recombination reaction.

Other factors, such as calcination temperature and phase compositions of NiO and TiO$_2$ in composite photocatalysts were also found to be very critical in determining the overall hydrogen yield. For investigating the role of calcination temperature and phase composition, in shaping the catalytic activity, composite samples of NiO and TiO$_2$ in 1:1 proportion were prepared by varying calcination conditions and the XRD patterns of these composites are shown in Fig. S6. The photocatalytic activities of corresponding samples are shown in Fig. 11. Both figures are explained in respective sections above. From the activity trend it is observed that activity increases with increase in crystallinity of the NiO and TiO$_2$ phases. Also, presence of secondary phase, NiTiO$_3$ has strongly affected the H$_2$ yield adversely. Thus, both crystallinity and presence of NiTiO$_3$ phase determines the overall H$_2$ yield. Among all samples NTC11 composite oxide shown in curve c of Fig.S6 was found to be the most active. This suggests that the synthetic conditions involving gel drying temperature of 90 °C and calcination at 600 °C for 10 h are the optimized conditions that offer a well crystalline *pn* nanojunction comprised of NiO and anatase TiO$_2$ phases (1:1) with minimal amount of NiTiO$_3$. Possibly, the concentration of Ni ions at the time of synthesis also has played an important role in restricting the conversion of anatase to rutile phase [22,41]. Rutile shows higher reactivity for crystallization of ilmenite phase or favoured the growth of NiTiO$_3$ than anatase phase [67]. Thus, slow heating of gel and availability of greater fraction of Ni ions during synthesis of NTC11, restricted the crystallization of adverse phase, NiTiO$_3$ and liberated the free NiO and TiO$_2$ phases, in contrast to what was observed in NTC36 where the reaction pathway leads to formation of substantial amounts of NiTiO$_3$ phase. Nickel titanate, NiTiO$_3$, was prepared by both sol-gel and solid state and both routes produced very low H$_2$ yield @ 15.2 and 2.2 μmol/g/h respectively, much lower than other samples in sunlight, thus verifying the fact that it is a poor photocatalyst. During our investigations on Ni doped indium titanate [31] as well as by others [28] it was observed that presence of NiTiO$_3$ as impurity phase even in small amounts degrades the photocatalytic activity of indium titanate. The crystal and electronic structure are responsible for poor activity. To understand the electronic structure, the first principles DFT based band structure calculations were performed on NiTiO$_3$ by us [31] and are briefly reiterated in Supplementary information, S1 as ready reference. It revealed that strong intermixing of Ni-*3d* with O-*2p* orbitals occurred in the valence band of NiTiO$_3$ and resulted in generation of a pseudo band gap at 1.36 eV. This pseudo band gap might act as hindrance and may contribute in weakening the intensity of electronic transition due to Ni^{2+} → Ti^{4+} charge transfer. The inactivity of ilmenite NiTiO$_3$ was also attributed to its structure consisting of a pseudo close packed hexagonal array of O^{2-} ions with two thirds of the octahedral sites of any basal plane occupied by identical cations in an ordered hexagonal net [40]. Owing to this geometry the oscillator strength for the charge transfer transitions, Ni^{2+} → Ti^{4+} becomes too weak to have an acceptable photoresponse in visible light. Also, it is reported [31,39,40] that inherently large particles of NiTiO$_3$ with low surface areas and pore volumes are produced by conventional synthetic procedures due to limitations of high reaction temperature and heterogeneous solid phase reactions. The presence of impurity ilmenite phase, NiTiO$_3$, more prominent in NTC36 than NTC11, will however, disrupt the *pn* junctions formed in the composite oxides, and may interrupt in the swift drive of charge carriers across the junctions.

To review our results, literature reports on Ni-Ti-O systems were surveyed and the most relevant ones for H$_2$ evolution are listed in Table-S7. Ni incorporated in TiO$_2$ in any form whether on surface by impregnation, or coupled with Titania as NiO or in form of cationic dopant substituting Ti^{4+} in Titania lattice, results in enhancement of activity. Dispersion of minor amounts of NiO on TiO$_2$ surface by wet

impregnation is commonly used strategy which has been adopted by most of researchers to enhance the hydrogen yield as there it acts as trap centres for electrons and sites for the photoreduction. Also, these trap centres formed on surface directs the photogenerated electrons to reach surface. Melian et al. [28] have modified the catalytic properties of TiO_2 by incorporating Ni and N both at the crystallographic sites of TiO_2 lattice and have reported H_2 yield of 260 µmol/h over 1 g of the most active oxide doped catalyst under fluorescent lamps. However, another approach in which both NiO and TiO_2 in substantial amounts is merged in a composite; offers efficient charge separation, by increasing the life of e^- and h^+ produced during the photoirradiation was entirely different, proceeding via altered mechanisms and had therefore renewed the interest. The improved photocatalytic properties of composites are by virtue of heterojunctions formed at the interfacial contact of dissimilar semiconductors of NiO and TiO_2. Li et al. [29] and Yu et al. [68] have investigated *pn* junctions in bicomponent composites and reported H_2 generation using mesoporous NiO/TiO_2 with 377 µmol/h/g and NiO/rGO/TiO_2 with 240 µmol/h/g respectively. Among all reports, catalysts used in our studies have shown comparatively better performance in the terms of H_2 yield (Table-S7), although it is pertinent to mention here that experimental conditions used for activity evaluation are not same. Here, a comprehensive comparison of the composites, NTC11, NTC36 with their component oxides and the secondary pure phase, $NiTiO_3$ which was found to coexist and was degrading the photocatalytic activity, under identical conditions is reported. Our results offer conversion rates under actual sunlight unlike most of the reports showing activity in UV light. With an aim to extend this work to a pilot plant, H_2 yield obtained over 100 mg of photocatalyst are extrapolated to more realistic extrapolation of per illumination area (m^2) in addition to per g (Table-S7). Most active photocatalyst, $Pt/NiO-TiO_2$ was found to generate photocatalytic H_2 @ of 1250 µmol/h/g or 1.4 l/h/m^2 with AQE of 7.8% under UV visible irradiation and 537 µmol/g/h or 0.6 l/h/m^2 under sunlight with AQE of 5.4% and SFE of 0.8%. The Ni-Ti composites were found to be cheap, active and stable photocatalysts and are therefore potential candidates for solar photocatalytic applications.

7. Conclusion

This study demonstrates the benefit of designing of *pn* junction from low cost and earth abundant NiO and TiO_2 for enhancing the photocatalytic H_2 evolution activity by tendering lower band gap energy and facilitating charge separation. Thus, NiO and TiO_2 in 1:1 ratio devoid of derogatory effect of $NiTiO_3$ phase are active, cheap and stable photocatalyst which can be projected as potential photocatalysts for actual large scale solar applications.

Acknowledgements

Appendix A. Supplementary data

Supplementary data associated with this article can be found, in the online version, at http://dx.doi.org/10.1016/j.apcatb.2017.09.004.

References

[1] A. Fujishima, K. Honda, Electrochemical photolysis of water at a semi-conductor electrode, Nature 238 (1972) 37–38.

[2] W.Y. Teoh, J.A. Scott, R. Amal, Progress in heterogeneous photocatalysis: from classical radical chemistry to engineering nanomaterials and solar reactors, J. Phys. Chem. Lett. 3 (2012) 629–639.

[3] K. Villa, X. Dome'nech, S. Malato, M.I. Maldonado, J. Peral, Heterogeneous photocatalytic hydrogen generation in a solar pilot plant, Int. J. Hydrogen Energy 38 (2013) 12718–12724.

[4] M.R. Pai, A.M. Banerjee, S.A. Rawool, A. Singhal, C. Nayak, S.H. Ehrman, A.K. Tripathi, S.R. Bharadwaj, A comprehensive study on sunlight driven photocatalytic hydrogen generation using low cost nanocrystalline Cu-Ti oxides, Solar Energy Mater. Solar Cells 154 (2016) 104–120.

[5] H.H. Park Kim, G. -h. Moon, W. Choi, Photoinduced charge transfer processes in solar photocatalysis based on modified TiO_2, Energy Environ. Sci. 9 (2016) 411–433.

[6] S.A. Ansari, M.M. Khan, M.O. Ansari, M.H. Cho, Nitrogen-doped titanium dioxide (N-doped TiO_2) for visible light photocatalysis, New J. Chem. 40 (2016) 3000–3009.

[7] F. Dong, S. Guo, H. Wang, X. Li, Z. Wu, Enhancement of the visible light photocatalytic activity of C-doped TiO_2 nanomaterials prepared by a green synthetic approach, J. Phys. Chem. C 115 (2011) 13285–13292.

[8] C. McManamon, J. O'Connell, P. Delaney, S. Rasappa, J.D. Holmes, M.A. Morris, A facile route to synthesis of S-doped TiO_2 nanoparticles for photocatalytic activity, J. Mol. Catal. A: Chem. 406 (2015) 51–57.

[9] F. Fresno, R. Portela, S. Súarez, J.M. Coronado, Photocatalytic materials: recent achievements and near future trends, J. Mater. Chem. A 2 (2014) 2863–2884.

[10] L. Li, P.A. Salvador, G.S. Rohrer, Photocatalysts with internal electric fields, Nanoscale 6 (2014) 24–42.

[11] X. Zhang, Q. Liu, Visible-light-induced degradation of formaldehyde over titania photocatalyst co-doped with nitrogen and nickel, Appl. Surf. Sci. 254 (2008) 4780–4785.

[12] J. Zhang, L. Qiao, J. Yu, Fabrication of NiS modified CdS nanorod p-n junction photocatalysts with enhanced visible-light photocatalytic H_2-production activity, Phys. Chem. Chem. Phys 15 (2013) 12088–12094.

[13] Y. Miyauchi, D. Nukui, Selective growth of n-type nanoparticles on p-type semiconductors for Z-scheme photocatalysis, ACS Appl. Mater. Interfaces 5 (19) (2013) 9770–9776.

[14] B. J. Cao, H. Xu, S. Chen Lin, Highly improved visible light photocatalytic activity of $BiPO_4$ through fabricating a novel p-n heterojunction $BiOI/BiPO_4$ nanocomposite, Chem. Eng. J. 228 (2013) 482–488.

[15] V.R. Choudhary, A.M. Rajput, A.S. Mamman, NiO-alkaline earth oxide catalysts for oxidative methane-to-syngas conversion: influence of alkaline earth oxide on the surface properties and temperature-programmed reduction/reaction by H_2 and methane, J. Catal. 178 (1998) 576–585.

[16] I. Hotovy, J. Huran, L. Spiess, S. Hascik, V. Rehacek, Preparation of nickel oxide thin films for gas sensors applications, Sens. Actuators B 57 (1–3) (1999) 147–152.

[17] X. Li, X. Zhang, Z. Li, Y. Qian, Synthesis and characteristics of NiO nanoparticles by thermal decomposition of nickel dimethylglyoximate rods, Solid State Commun. 137 (2006) 581–584.

[18] C.-J. Chen, C.-H. Liao, K.-C. Hsu, Y.-T. Wu, J.C.S. Wu, P-N junction mechanism on improved NiO/TiO_2, Photocatalyst Catal. Commun. 12 (2011) 1307–1310.

[19] K.-j. Zhang, W. Xu, X.-j. Li, S.-j Zheng, G. Xu, J.-h Wang, Photocatalytic oxidation activity of titanium dioxide film enhanced by Mn non-uniform doping, Trans. Nonferrous Met. Soc. China 16 (2006) 1069–1075.

[20] H. Lin, H. Ye, B. Xu, J. Cao, S. Chen, Ag_3PO_4 quantum dot sensitized $BiPO_4$: a novel p-n junction $Ag_3PO_4/BiPO_4$ with enhanced visible-light photocatalytic activity, Catal. Commun. 37 (2013) 55–59.

[21] T. Sreethawong, S. Ngamsinlapasathian, S. Yoshikawa, Surfactant-aided sol-gel synthesis of mesoporous-assembled TiO_2-NiO mixed oxide nanocrystals and their photocatalytic azo dye degradation activity, Chem. Eng. J. 192 (2012) 292–300.

[22] Y. Ku, C.-N. Lin, W.-M. Hou, Characterization of coupled NiO/TiO_2 photocatalyst for the photocatalytic reduction of Cr(VI) in aqueous solution, J. Mol. Catal. A: Chem. 349 (2011) 20–27.

[23] Z. Shifu, L. Sujuan, Preparation and activity evaluation of p-n junction photocatalyst NiO/TiO_2, J. Hazard. Mater. 155 (2008) 320–326.

[24] J. Yu, W. Wang, B. Cheng, Synthesis and enhanced photocatalytic activity of a hierarchical porous flowerlike p-n junction NiO/TiO_2 photocatalyst, Chem. Asian J. 5 (2010) 2499–2506.

[25] H. Hu, W.-j. Xiao, J. Yuan, J.-w. Shi, M.-x. Chen, W.-f. Shang Guan, Preparations of TiO_2 film coated on foam nickel substrate by sol-gel processes and its photocatalytic activity for degradation of acetaldehyde, J. Environ. Sci. 19 (2007) 80–85.

[26] D. Jing, Y. Zhang, L. Guo, Study on the synthesis of Ni doped mesoporous TiO_2 and its photocatalytic activity for hydrogen evolution in aqueous methanol solution, Chem. Phys. Lett. 415 (2005) 74–78.

[27] R. Liu, H. Yoshida, S. Fujita, M. Arai, Photocatalytic hydrogen production from glycerol and water with NiO_x/TiO_2 catalysts, Appl. Catal. B: Environ. 144 (2014) 41–45.

[28] E.P. Melián, M.N. Suárez, T. Jardiel, J.M.D. Rodríguez, A.C. Caballero, J. Arãna, D.G. Calatayud, O.G. Díaz, Influence of nickel in the hydrogen production activity of TiO_2, Appl. Catal. B: Environ. 152–153 (2014) 192–201.

[29] L. Li, B. Cheng, Y. Wang, J. Yu, Enhanced photocatalytic H_2-production activity of bicomponent NiO/TiO_2 composite nanofibers, J. Colloid Interface Sci. 449 (2015) 115–121.

[30] M.R. Pai, A.M. Banerjee, S.R. Bharadwaj, Effect of transition metal ion doping on photocatalytic properties of In–Ti oxides, J. Mater. Res. 30 (21) (2015) 3259–3266.

[31] A.M. Banerjee, M.R. Pai, A. Arya, S.R. Bharadwaj, Photocatalytic H_2 generation over In_2TiO_5, Ni substituted In_2TiO_5 and $NiTiO_3$—a combined theoretical and experimental study, RSC Adv. 5 (2015) 61218–61229.

[32] M.R. Pai, J. Majeed, A.M. Banerjee, A. Arya, S. Bhattacharya, R. Rao, S.R. Bharadwaj, Role of Nd³⁺ ions in modifying the band structure and photocatalytic properties of substituted indium titanates, In₂₍₁₋ₓ₎Nd₂ₓTiO₅ oxides, J. Phys. Chem. C 116 (2012) 1458–1471.

[33] M.R. Pai, A.M. Singhal, A.M. Banerjee, R. Tewari, G.K. Dey, A.K. Tyagi, S.R. Bharadwaj, Synthesis, characterization and photocatalytic H₂ generation over ternary indium titanate nanoparticles, J. Nanosci. Nanotechnol. 12 (2012) 1957–1966.

[34] M.R. Pai, A.M. Banerjee, A.K. Tripathi, S.R. Bharadwaj, S. Banerjee, A.K. Tyagi (Eds.), Functional Materials: Preparations, Processing and Applications, Elsevier, USA, 2012, pp. 579–606.

[35] R.A. Spurr, H. Myers, Quantitative analysis of anatase-rutile mixtures with an X-ray diffractometer, Anal. Chem. 29 (1957) 760–762.

[36] D.J. Taylor, P.F. Fleig, R.A. Page, Characterization of nickel titanate synthesized by sol–gel processing, Thin Solid Films 408 (2002) 104–110.

[37] M.A. Ruiz-Preciado, A. Kassiba, A. Gibaud, A. Morales-Acevedo, Comparison of nickel titanate (NiTiO₃) powders synthesized by sol–gel and solid state reaction, Mater. Sci. Semicond. Process. 37 (2015) 171–178.

[38] T.−I. Chang, J.−L. Huang, J.−P. Lin, S.−C. Wang, H.−H. Lu, L. Wu, J.-F. Lin, Effect of drying temperature on structure, phase transformation of sol–gel-derived lead zirconate titanate powders, J. Alloys Compd. 414 (2006) 224–229.

[39] Y.M. Chiang, D. Birnie, W.D. Kingery, Physical Ceramics Principles of Ceramic Science and Engineering, John Wiley & Sons Inc, New York, 1996.

[40] Y. Ni, X. Wang, J. Hong, Nickel titanate microtubes constructed by nearly spherical nanoparticles: Preparation, characterization and properties, Mater. Res. Bull. 44 (2009) 1797–1801.

[41] M.R. Mohammadi, D.J. Fray, Mesoporous and nanocrystalline sol–gel derived NiTiO₃ at the low temperature: controlling the structure, size and surface area by Ni:Ti molar ratio, Solid State Sci. 12 (2010) 1629–1640.

[42] T. Ohsaka, F. Izumi, Y. Fujiki, Raman spectrum of anatase, TiO₂, J. Raman Spectrosc. 7 (1978) 321–324.

[43] N. Mironova-Ulmane, A. Kuzmin, J. Grabis, I. Sildos, V.I. Voronin, I.F. Berger, V.A. Kazantsev, Structural and magnetic properties of nickel oxide nanopowders, Solid State Phenom. 168–169 (2011) 341–344.

[44] K.P. Lopes, L.S. Cavalcante, A.Z. Simões, J.A. Varela, E. Longo, E.R. Leite, NiTiO₃ powders obtained by polymeric precursor method: synthesis and characterization, J. Alloys Compd. 468 (2009) 327–332.

[45] P.H.M. de Korte, G. Blasse, Water photoelectrolysis using nickel titanate and niobate as photoanodes, J. Solid State Chem. 44 (1982) 150–155.

[46] Y.-J. Lin, Y.-H. Chang, W.-D. Yang, B.-S. Tsai, Synthesis and characterization of ilmenite NiTiO₃ and CoTiO₃ prepared by a modified Pechini method, J. Non-Cryst. Solids 352 (2006) 789–794.

[47] E. Wang, T. He, L. Zhao, Y. Chen, Y. Cao, Improved visible light photocatalytic activity of titania doped with tin and nitrogen, J. Mater. Chem. 21 (2011) 144–150.

[48] J. Schneider, M. Matsuoka, M. Takeuchi, J. Zhang, Y. Horiuchi, M. Anpo, D.W. Bahnemann, Understanding TiO₂ photocatalysis: mechanisms and materials, Chem. Rev. 114 (2014) 9919–9986.

[49] J. Yan, G. Wu, N. Guan, L. Li, Z. Li, X. Cao, Understanding the effect of surface/bulk defects on the photocatalytic activity of TiO₂: anatase versus rutile, Phys. Chem. Chem. Phys. 15 (2013) 10978–10988.

[50] T. Ahmad, K.V. Ramanujachary, S.E. Lofland, A.K. Ganguli, Magnetic and electrochemical properties of nickel oxide nanoparticles obtained by the reverse-micellar route, Solid State Sci. 8 (2006) 425–430.

[51] T. Sreethawong, Y. Suzuki, S. Yoshikawa, Photocatalytic evolution of hydrogen over mesoporous TiO₂ supported NiO photocatalyst prepared by single-step sol–gel process with surfactant template, Int. J. Hydrogen Energy 30 (2005) 1053–1062.

[52] K.S. Kim, R.E. Davis, Electron spectroscopy of the nickel-oxygen system, J. Electron Spectros. Relat. Phenom. 1 (1972–1973) 251–258.

[53] M.A. van Veenendaal, G.A. Sawatzky, Nonlocal screening effects in 2p X-ray photoemission spectroscopy core-level line shapes of transition metal compounds, Phys. Rev. Lett. 70 (1993) 2459–2462.

[54] B. Erdem, R.A. Hunsicker, G.W. Simmons, E.D. Sudol, V.L. Dimonie, M.S. El-Aasser, XPS and FTIR surface characterization of TiO₂ particles used in polymer encapsulation, Langmuir 17 (2001) 2664–2669.

[55] Y. Qu, W. Zhou, Z. Ren, S. Du, X. Meng, G. Tian, K. Pan, G. Wang, H. Fu, Facile preparation of porous NiTiO₃ nanorods with enhanced visible-light-driven photocatalytic performance, J. Mater. Chem. 22 (2012) 16471–16476.

[56] K.S. Kim, N. Winograd, X-ray photoelectron spectroscopic studies of nickel-oxygen surfaces using oxygen and argon ion-bombardment, Surf. Sci. 43 (1974) 625–643.

[57] K.M. Parida, S. Ku Mahanta, S. Martha, A. Nashim, Fabrication of NiO/Ta₂O₅ composite photocatalyst for hydrogen production under visible light, Int. J. Energy Res. 37 (2013) 161–170.

[58] M. Landmann, E. Rauls, W.G. Schmidt, The electronic structure and optical response of rutile, anatase and brookite TiO₂, J. Phys.: Condens. Matter 24 (2012) 6 195503.

[59] P. Liao, E.A. Carter, New concepts and modeling strategies to design and evaluate photo-electro-catalysts based on transition metal oxides, Chem. Soc. Rev. 42 (2013) 2401–2422.

[60] M.C. Toroker, E.A. Carter, Transition metal oxide alloys as potential solar energy conversion materials, J. Mater. Chem. A 1 (2013) 2474–2484.

[61] M.C. Toroker, D.K. Kanan, N. Alidoust, L.Y. Isseroff, P. Liao, E.A. Carter, First principles scheme to evaluate band edge positions in potential transition metal oxide photocatalysts and photoelectrodes, Phys. Chem. Chem. Phys. 13 (2011) 16644–16654.

[62] S. Hufner, Electronic structure of NiO and related 3d-transition-metal compounds, Adv. Phys. 43 (1994) 183–356.

[63] F. Reinert, P. Steiner, S. Hufner, H. Schmitt, J. Fink, M. Knupfer, P. Sandl, E. Bertel, Electron and hole doping in NiO, Z. Phys. B: Condens. Matter 97 (1995) 83–93.

[64] W.-L. Jang, Y.-M. Lu, W.-S. Hwang, W.-C. Chen, Electrical properties of Li-doped NiO films, J. Eur. Ceram. Soc. 30 (2010) 503–508.

[65] P. Kuiper, G. Kruizinga, J. Ghijsen, G.A. Sawatzky, H. Verweij, Character of holes in LiₓNi₁₋ₓO and their magnetic behaviour, Phys. Rev. Lett. 62 (1989) 221–224.

[66] Y. Huang, Q. Zhang, J. Xi, Z. Ji, Transparent conductive p-type lithium-doped nickel oxide thin films deposited by pulsed plasma deposition, Appl. Surf. Sci. 258 (2012) 7435–7439.

[67] D.B. Goldman, Mechanism and kinetics of reactions in the system Ni-Ti-O, J. Am. Ceram. Soc. 66 (1983) 811–814.

[68] X. Yu, J. Zhang, Z. Zhao, W. Guo, J. Qiu, X. Mou, A. Li, J.P. Claverie, H. Liu, NiO-TiO₂ p-n heterostructured nanocables bridged by zero-bandgap rGO for highly efficient photocatalytic water splitting, Nano Energy 16 (2015) 207–217.